



HAL
open science

The Pristine Inner Galaxy Survey (PIGS) IV: A photometric metallicity analysis of the Sagittarius dwarf spheroidal galaxy

Sara Vitali, Anke Arentsen, Else Starckenburg, Paula Jofré, Nicolas F. Martin, David S. Aguado, Raymond Carlberg, Jonay I. González Hernández, Rodrigo Ibata, Georges Kordopatis, et al.

► To cite this version:

Sara Vitali, Anke Arentsen, Else Starckenburg, Paula Jofré, Nicolas F. Martin, et al.. The Pristine Inner Galaxy Survey (PIGS) IV: A photometric metallicity analysis of the Sagittarius dwarf spheroidal galaxy. *Monthly Notices of the Royal Astronomical Society*, 2022, 10.1093/mnras/stac2869 . insu-03820720

HAL Id: insu-03820720

<https://insu.hal.science/insu-03820720v1>

Submitted on 23 Mar 2023

HAL is a multi-disciplinary open access archive for the deposit and dissemination of scientific research documents, whether they are published or not. The documents may come from teaching and research institutions in France or abroad, or from public or private research centers.

L'archive ouverte pluridisciplinaire **HAL**, est destinée au dépôt et à la diffusion de documents scientifiques de niveau recherche, publiés ou non, émanant des établissements d'enseignement et de recherche français ou étrangers, des laboratoires publics ou privés.

The Pristine Inner Galaxy Survey (PIGS) – IV. A photometric metallicity analysis of the Sagittarius dwarf spheroidal galaxy

Sara Vitali ¹★, Anke Arentsen ²★, Else Starkenburg ³★, Paula Jofré ¹, Nicolas F. Martin ^{2,4}, David S. Aguado ^{5,6}, Raymond Carlberg ⁷, Jonay I. González Hernández ^{8,9}, Rodrigo Ibata ², Georges Kordopatis ¹⁰, Khyati Malhan ⁴, Pau Ramos ², Federico Sestito ¹¹, Zhen Yuan ², Sven Buder ^{12,13}, Geraint F. Lewis ¹⁴, Zhen Wan ¹⁵ and Daniel B. Zucker ^{16,17}

¹Núcleo de Astronomía & Millenium Nucleus ERIS, Facultad de Ingeniería y Ciencias Universidad Diego Portales, Ejército 441, Santiago, Chile

²Université de Strasbourg, CNRS, Observatoire astronomique de Strasbourg, UMR 7550, F-67000 Strasbourg, France

³Kapteyn Astronomical Institute, University of Groningen, Postbus 800, NL-9700 AV, Groningen, the Netherlands

⁴Max-Planck-Institut für Astronomie, Königstuhl 17, D-69117 Heidelberg, Germany

⁵Dipartimento di Fisica e Astronomia, Università degli Studi di Firenze, Via G. Sansone 1, I-50019 Sesto Fiorentino, Italy

⁶INAF/Osservatorio Astrofisico di Arcetri, Largo E. Fermi 5, I-50125 Firenze, Italy

⁷Department of Astronomy & Astrophysics, University of Toronto, Toronto, ON M5S 3H4, Canada

⁸Instituto de Astrofísica de Canarias (IAC), E-38200 La Laguna, Tenerife, Spain

⁹Universidad de La Laguna, Dept. Astrofísica, E-38206 La Laguna, Tenerife, Spain

¹⁰Université Côte d'Azur, Observatoire de la Côte d'Azur, CNRS, Laboratoire Lagrange, Boulevard de l'Observatoire CS 34229 - F 06304 NICE Cedex 4, France

¹¹Department of Physics and Astronomy, University of Victoria, PO Box 3055, STN CSC, Victoria BC V8W 3P6, Canada

¹²Research School of Astronomy & Astrophysics, Australian National University, ACT 2611, Australia

¹³Center of Excellence for Astrophysics in Three Dimensions (ASTRO-3D), Mount Stromlo Rd Stromlo, Australian Capital Territory 2611, Australia

¹⁴Sydney Institute for Astronomy, School of Physics, A28, The University of Sydney, NSW 2006, Australia

¹⁵School of Astronomy and Space Science, University of Science and Technology of China, Hefei, Anhui 230026, China

¹⁶Department of Physics and Astronomy, Macquarie University, Sydney, NSW 2109, Australia

¹⁷Macquarie University Research Centre for Astronomy, Astrophysics & Astrophotonics, Sydney, NSW 2109, Australia

Accepted 2022 September 17. Received 2022 September 13; in original form 2022 April 25

ABSTRACT

We present a comprehensive metallicity analysis of the Sagittarius dwarf spheroidal galaxy (Sgr dSph) using *Pristine CaHK* photometry. We base our member selection on *Gaia* EDR3 astrometry, applying a magnitude limit at $G_0 = 17.3$, and our population study on the metallicity-sensitive photometry from the *Pristine* Inner Galaxy Survey (PIGS). Working with photometric metallicities instead of spectroscopic metallicities allows us to cover an unprecedented large area (~ 100 square degrees) of the dwarf galaxy, and to study the spatial distribution of its members as function of metallicity with little selection effects. Our study compares the spatial distributions of a metal-poor population of 9719 stars with $[\text{Fe}/\text{H}] < -1.3$ and a metal-rich one of 30 115 stars with $[\text{Fe}/\text{H}] > -1.0$. The photometric Sgr sample also allows us to assemble the largest sample of 1150 very metal-poor Sgr candidates ($[\text{Fe}/\text{H}] < -2.0$). By investigating and fitting the spatial properties of the metal-rich and metal-poor population, we find a negative metallicity gradient which extends up to 12 degrees from the Sgr centre (or ~ 5.5 kpc at the distance of Sgr), the limit of our footprint. We conclude that the relative number of metal-poor stars increases in the outer areas of the galaxy, while the central region is dominated by metal-rich stars. These findings suggest an outside-in formation process and are an indication of the extended formation history of Sgr, which has been affected by the tidal interaction between Sgr and the Milky Way.

Key words: galaxies: dwarf – Local Group – galaxies: stellar content.

1 INTRODUCTION

The variety of galaxies present in the Universe, with their different shapes, features and sizes, suggests the existence of several formation processes behind galactic structures. Due to the mutual gravitational attractions, mergers have led to the formation of bigger structures.

It has been widely acknowledged that satellite galaxies have been accreting on to the Milky Way (MW; see for a review e.g. Bullock & Johnston 2005; Bland-Hawthorn & Gerhard 2016). The dwarf galaxies that orbit around the MW are insightful laboratories to learn about the early evolution of our Galaxy, as they are relics of the main building blocks of the Galactic halo (Frebel & Bromm 2012).

The Sagittarius dwarf spheroidal galaxy (Sgr dSph) is one of such galaxies, discovered by Ibata, Gilmore & Irwin (1994) in the direction of the Galactic bulge. It is one of the biggest dwarf galaxies known around the MW, with an estimated stellar mass of $\sim 4.8 \times 10^8 M_\odot$.

* E-mail: sara.vitali@mail.udp.cl (SV); anke.arentsen@ast.cam.ac.uk (AA); estarkenburg@astro.rug.nl (ES)

(Vasiliev & Belokurov 2020), and among the most luminous with $M_V \sim -15.1/-15.5$ (Niederste-Ostholt et al. 2010). Its core is located on the opposite side of the Galactic centre, at a relatively nearby heliocentric distance of ≈ 26.5 kpc (Monaco et al. 2004; Ferguson & Strigari 2020; Vasiliev & Belokurov 2020). Sgr is a compelling example of an ongoing merger with the MW, in which the system is being disrupted by the tidal interaction with our Galaxy (Ibata 1997; Mateo, Olszewski & Morrison 1998; Belokurov et al. 2014), with the first in-fall occurring about 5 Gyr ago (Ruiz-Lara et al. 2020). Many of its stars have been stripped away from the core in long tidal streams (Ibata et al. 2001; Majewski et al. 2003; Law & Majewski 2010) that wrap around the MW. Despite its inevitable destruction, the core of the Sgr dwarf galaxy is still visible. However, the projected proximity to the Galactic bulge has made the study of the dSph galaxy challenging due to the contamination from MW foreground stars and extinction by interstellar dust.

With its history of tidal disruption, Sgr is a unique workshop for examining the physical aspects connected to the chemical evolution from the perspective of the hierarchical galaxy formation scenario. In recent years, a number of studies has been dedicated to disentangle the complex Sgr star formation history (SFH), based either on high-resolution spectroscopy (e.g. Bonifacio et al. 2000; Smecker-Hane & McWilliam 2002; Monaco et al. 2005; Sbordone et al. 2005; Chou et al. 2007; McWilliam, Wallerstein & Mottini 2013; Hasselquist et al. 2017; Hansen et al. 2018) or photometric techniques (Bellazzini, Ferraro & Buonanno 1999b; Layden & Sarajedini 2000; Siegel et al. 2007). They found that Sgr has experienced many bursts of star formation that resulted in stellar populations with different ages and metallicities. These are described in detail for instance in the work of Siegel et al. (2007), in which the monotonically varying age-metallicity distribution consists of four different populations: a dominant intermediate-age stellar population aged $\sim 4-8$ Gyr with $-0.6 \lesssim [\text{Fe}/\text{H}] \lesssim -0.4$, a younger and more metal-rich (MR) stellar population of 2–3 Gyr old with $[\text{Fe}/\text{H}] \sim -0.1$, a small population younger than 2 Gyr with super-solar metallicities ($[\text{Fe}/\text{H}] \sim +0.5$), and a metal-poor (MP) population with $[\text{Fe}/\text{H}] \sim -1.2$ and ages >10 Gyr.

Sgr is one of the most massive satellite galaxies around the MW, after the Large Magellanic Cloud and Small Magellanic Cloud. The stellar mass-metallicity relation for dwarf galaxies predicts that more massive galaxies show higher average metallicity (Kirby et al. 2013). The predominance of a relatively MR population in the Sgr core (with the bulk of the stars having an average $[\text{Fe}/\text{H}] \sim -0.5$, Monaco et al. 2003; Siegel et al. 2007; Mucciarelli et al. 2017) makes the identification and study of MP stars particularly difficult. Sgr does also host an old and MP component ($[\text{Fe}/\text{H}] < -1.0$ and age ~ 10 Gyr, Monaco et al. 2003; Siegel et al. 2007; Bellazzini et al. 2008), but to date, only ~ 20 very MP (VMP, $[\text{Fe}/\text{H}] < -2.0$) Sgr stars have been discovered and studied with either high- or low-resolution spectroscopy (Bellazzini et al. 2008; Mucciarelli et al. 2017; Hansen et al. 2018; Chiti & Frebel 2019; Chiti, Hansen & Frebel 2020). This VMP population in Sgr has important implications when studying galaxy evolution. They are archaeological fossils from the earliest time which will unveil the primitive stellar populations in the Sgr dwarf galaxy. One theoretical expectation is that smaller dwarf systems may have contributed to the formation of more massive ones, which could have happened to Sagittarius (Chiti et al. 2020). A recent work by Malhan et al. (2022) found that the MP Elqui stream is associated with Sagittarius and was likely accreted inside the Sgr dSph.

Studying the spatial distribution of different stellar populations is key, because it helps us to understand the various episodes of

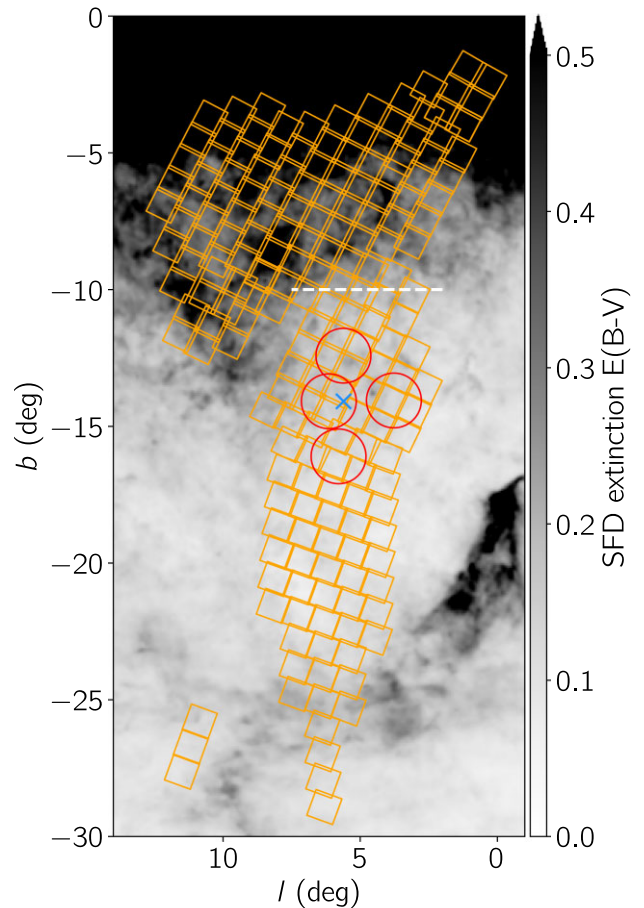


Figure 1. The photometric fields of the Southern PIGS photometric footprint are shown in orange, with the Sgr extension present below the white dashed line at $b = -10$. The four red circles indicate fields with dedicated Sgr spectroscopic follow-up in PIGS. The extinction map is from Schlegel, Finkbeiner & Davis (1998), where for the sake of contrast we fix the upper limit of the colour bar at 0.5. The location of M54 has been highlighted with a blue cross.

star formation which have occurred during the evolution of Sgr. The correlation of the present spatial distributions of populations of different metallicities and ages provides hints about the primitive distribution of the gas from which they formed. Using chemical abundances of a sample of Sgr stars, Mucciarelli et al. (2017) revealed a metallicity gradient inside the core of the dwarf galaxy, supporting the hypothesis of a complex SFH. How the evolution of the galaxy has affected the spatial distribution of the different stellar populations is still an open debate, which needs more extended and comprehensive samples, and especially for the more MP component. For this purpose, one would ideally have a large, homogeneous, and clean sample of Sgr stars with available metallicities.

The incredible data collected by the Gaia mission, and especially the arrival of the high-accuracy *Gaia* EDR3 astrometry (Gaia Collaboration 2021), allow for the building of a robust sample of Sgr member stars. Relying on photometric metallicities instead of spectroscopic metallicities allows the use of a much larger and more homogeneous sample to investigate the global metallicity structure of the galaxy. In this context, a great data set is the photometric *Pristine* Inner Galaxy Survey (PIGS; Arentsen et al. 2020), consisting of metallicity-sensitive *CaHK* photometry of stars in the MW bulge region. PIGS includes a region focused on Sgr,

from the highest-density area of the system until the onset of its tidal stream.

This paper is devoted to a photometric metallicity analysis of the Sgr galaxy, carried out thanks to the combination of the *Gaia* astrometry and broad-band photometry and the PIGS metallicity-sensitive *CaHK* photometry which cover about 100 square degrees of Sgr. The data and the member selection are presented in Section 2. The combination of *Gaia* and *Pristine* leads to an unprecedented large Sgr sample of 44 785 stars with $G_0 < 17.3$ with available metallicity information, enabling a wide investigation of the spatial distributions of the stellar populations with different metallicities hosted in Sgr. We analysed the different spatial distributions of populations of different metallicities ($[\text{Fe}/\text{H}] < -2.0$, < -1.3 and > -1.0) in Section 3, and present a large sample of 1150 new very MP candidates. We study the metallicity gradient, which extends to at least $\sim 12^\circ$ from the centre of the Sgr remnant. Our approach is very effective in characterizing the metallicity structure of Sgr. We discuss what our results can teach us about the (early) evolution of the Sagittarius system in Section 4, and finish with conclusions and a discussion of future prospects in Section 5.

2 DATA

2.1 Photometry

In this paper, we use the PIGS photometry in the Sgr region, see Fig. 1. The *Pristine* survey (of which PIGS is an extension) has been ongoing since 2016 (Starkenburg et al. 2017) and has the main goal to search for and study the most MP stars in and around the MW. It makes use of the narrow-band *CaHK* filter designed for MegaCam mounted on the Canada-France-Hawaii Telescope (CFHT), which covers the Ca II H&K absorption lines that are sensitive probes of stellar metallicity. The targeting of MP stars in the main *Pristine* halo survey has been extremely efficient (Youakim et al. 2017; Aguado et al. 2019), and this efficiency has been demonstrated in the inner Galaxy as well (Arentsen et al. 2020). The Sgr extension of PIGS has not been used before, and we present it here for the first time.

2.1.1 Photometric field-to-field calibration

The data reduction proceeds as in Starkenburg et al. (2017) until the field-to-field calibration step. Fig. 1 presents each of the observed *CaHK* MegaCam images in our footprint (orange squares), which may have slightly different zero-points of the order of a few tenths of a magnitude. In the main *Pristine* halo survey, fields were calibrated with respect to each other by determining *CaHK* offsets using the red part of the stellar locus of a *CaHK*–SDSS colour–colour diagram (see fig. 7 of Starkenburg et al. 2017). This part of the locus mostly consists of nearby dwarf stars. For this calibration, the photometry needs to be dereddened, which was done using the same reddening map for the halo survey, i.e. the Schlegel dust map, hereafter SFD (Schlegel et al. 1998) map. This map contains the integrated reddening along the line of sight, which may be different than the actual reddening to the nearby dwarfs used for the calibration. Towards the halo, this difference is small and has not been taken into account. Towards Sgr, however, the reddening could be expected to change significantly as function of distance to the stars because we are looking through a large part of the disc, and we should not use the integrated SFD reddening. We therefore devised a new field-to-field calibration strategy specifically for the PIGS Sgr footprint ($b < -10$ degree).

Instead of using only the red part of the stellar locus, we use the full *CaHK*–*Gaia* stellar locus of nearby dwarfs and simultaneously fit

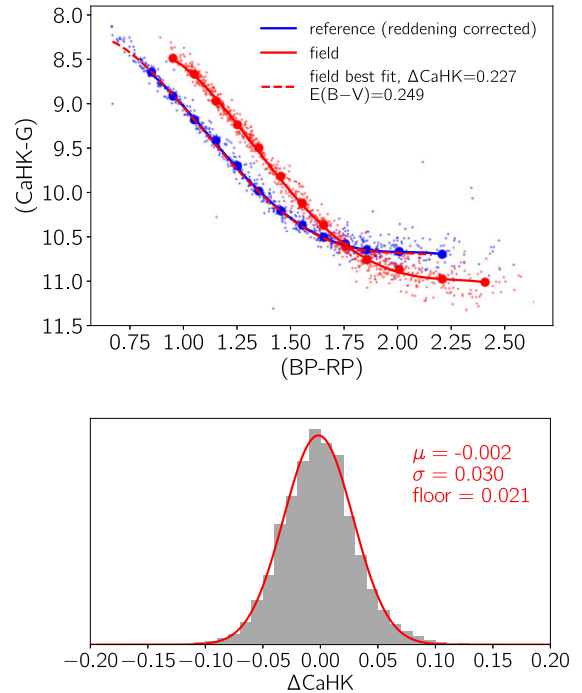


Figure 2. Field-to-field calibration of the PIGS-Sgr footprint. Top panel: stellar locus used for the calibration, with the reference field in blue and an example field to calibrate in red. Large points indicate the median ($CaHK - G$) values in bins of $(BP - RP)$, the solid lines are fourth order polynomials fitted through the medians. The red-dotted line indicates the best fit, with the best $\Delta CaHK$ and $E(B-V)$ indicated. Bottom panel: difference in $CaHK$ for all pairs of observations of a given star on two different MegaCam fields, for all fields in the Sgr footprint. The mean μ , standard deviation σ , and uncertainty floor $\sigma/\sqrt{2}$ are indicated.

for the *CaHK* offset (shifting the locus by a constant) and the average foreground $E(B-V)$ for each field (changing the shape of the locus). We select dwarf stars ($M_G < 4$) with *CaHK* uncertainties < 0.15 mag, parallax uncertainties < 20 per cent, and distances roughly between 500 and 1000 pc (from the *Gaia* parallaxes) as to not span too large a range in distances. We apply additional quality cuts to the astrometry ($RUWE < 1.2$, this is stricter than the cut we apply in Section 2.2, because we aim for higher quality for the calibration) and the photometry (the same cuts on $BP-RP$ excess factor and variability as discussed in Section 2.2) to get to the final calibration sample.

We select a field with relatively low $E(B-V)_{\text{SFD}}$ at $(l, b) = (6.25^\circ, -21.2^\circ)$ as the reference field, and correct it for extinction using the integrated SFD map (which is likely not too bad 20 degrees away from the Galactic plane) with the filter coefficients as described in the next subsection. We take the median $(CaHK - G)_0$ in bins in $(BP - RP)_0$ of 0.1 (or 0.2 in the reddest part), requiring at least five stars per bin, and fit a fourth-order polynomial to it. We do the same in each field to be calibrated, but for the reddened colours. We then compute the χ^2 for a grid of $\Delta CaHK$ and $E(B-V)$ and adopt the best solution. We show the stellar locus of the reference field and an example field with its best fit in the top panel of Fig. 2.

We test the quality of our calibration by determining the difference in *CaHK* for all stars in the Sgr footprint observed on two different images, possible thanks to the overlap between fields. Taking only stars with *CaHK* uncertainties less than 0.01, we infer a dispersion of 0.03 mag implying an uncertainty floor of 0.021 (dividing the dispersion by $\sqrt{2}$), see the bottom panel of Fig. 2. This is comparable to the uncertainty floor estimated for the main survey (0.02 mag;

Starkenburger et al. 2017) and corresponds to a metallicity uncertainty of ~ 0.15 dex in our methodology (see Section 3).

2.1.2 Catalogue

We cross-match the PIGS photometry with the astrometric data from *Gaia* EDR3 (Gaia Collaboration 2021), from which we use parallaxes and proper motions to perform a selection to isolate the member of Sgr (see Section 2.2). We also use the *Gaia* broad-band photometry combined with the PIGS photometry to select stars of different metallicities (see Section 3.2). Throughout this paper, we only use data cross-matched with the PIGS + *Gaia* catalogue for Sgr.

We correct for dust extinction using the SFD map. We use the colour-dependent extinction coefficients for the *Gaia* EDR3 filters from Casagrande et al. (2021; adopting the ‘FSF’ extinction law) and 3.924 for *CaHK* (Starkenburger et al. 2017).

2.2 Member selection

Establishing proper criteria to define the membership of stars to a dwarf galaxy is a crucial and challenging step. Sgr is highly affected by the contamination coming from different Galactic populations, namely the Galactic bulge, the thick disc and the thin disc (Ibata et al. 1997), and the Galactic halo. It is necessary to find an accurate balance between reducing MW contamination and not losing too many Sgr candidates.

We apply the following cuts to obtain Sgr members from our PIGS + *Gaia* catalogue. We only consider the part of the PIGS footprint with $b < -10^\circ$, to avoid the region close to the Galactic plane which will have more contamination. We isolate Sgr candidates using a cut on the parallax to remove foreground stars ($|\varpi| \leq 2\epsilon_\varpi$). We limit our analysis to stars with $G_0 \leq 17.3$ to avoid fainter stars for which the uncertainties on the *Gaia* astrometry and the *CaHK* photometry become too large. Additionally, helium-burning (red clump and horizontal branch) stars start to contribute significantly at fainter magnitudes. Deriving photometric metallicities for the (bluer) horizontal branch is more difficult since the metallicity sensitivity of *Pristine* reduces for hotter stars; our spectroscopic training sample (see the next section) does not include horizontal branch stars and some of the stars on the horizontal branch are photometrically variable. Excluding these bluer (more MP) stars while including the (more MR) red clump stars would bias our sample against MP stars. This is another reason to limit the analysis to brighter stars only. This leads to a sample of $\sim 52\,000$ stars. We apply additional quality cuts on $\text{RUWE} (< 1.4)$, $\text{astrometric_excess_noise_sig} (\leq 2)$ as described in Lindegren et al. (2021), and the fidelity flag (> 0.5) from Rybizki et al. (2022).

We constrained the photometric variability for the *Gaia* photometry using the *Gaia* catalogue parameters phot_g_n_obs (the number of observations in the G-band) and $\text{phot_g_mean_flux_over_error}$ (the mean flux over the error in the G-band), following equations 17 and 18 of Fernández-Alvar et al. (2021). We further clean the sample using the BP–RP flux excess: $|C_*| \leq 3\sigma_{C_*}(G)$ (Riello et al. 2021). These two last refinements remove 1.3 per cent of the previous selection. We finally defined the Sgr members with a cut on the proper motions (PMs), as shown in Fig. 3. We select stars within a radius of 0.6 mas yr^{-1} of the mean PM of Sgr, corrected for its variation with RA and Dec. as reported in the work (Vasiliev & Belokurov 2020) using the

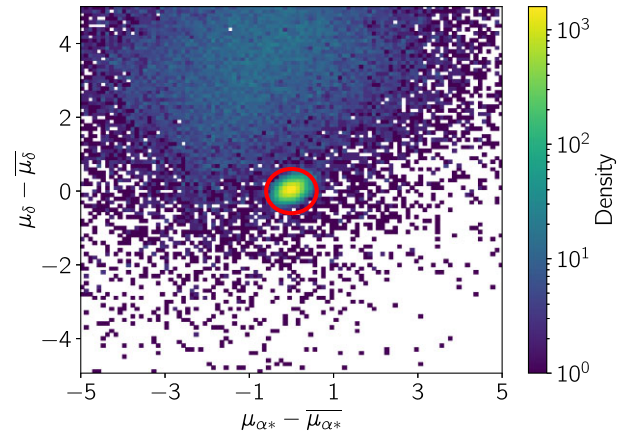


Figure 3. Zoom in the distribution of the proper motion values derived from *Gaia* EDR3 (Gaia Collaboration 2021) for the PIGS data set after having isolated the Sgr candidates. These PM values are subtracted from the mean PM of the Sgr members ($\overline{\mu_{\alpha^*}}$), following expression (4) from Vasiliev & Belokurov (2020). The Sgr galaxy is visible as a clear over-density centred at 0. We select Sgr stars within a radius of 0.6 mas yr^{-1} , delimited by the red circle.

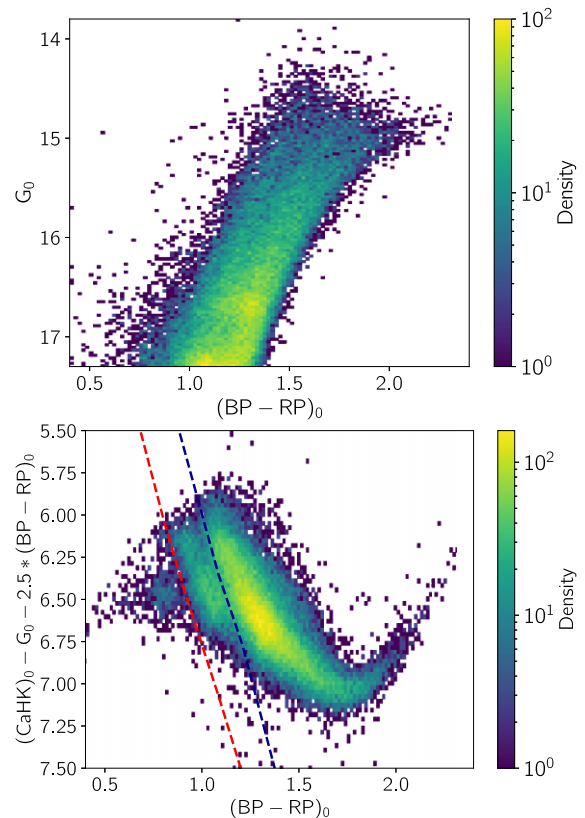


Figure 4. *Top:* colour–magnitude diagram with *Gaia* photometry for the Sgr selected members after applying all the cuts described in the text. *Bottom:* colour–colour diagram of the same Sgr selection. The y-axis includes the metallicity-dependent *CaHK* term. We identified stars below the red dashed line as MW contamination, and removed them from the Sgr sample. The blue line delimits the Sgr helium-burning red clump sequence from the normal giants.

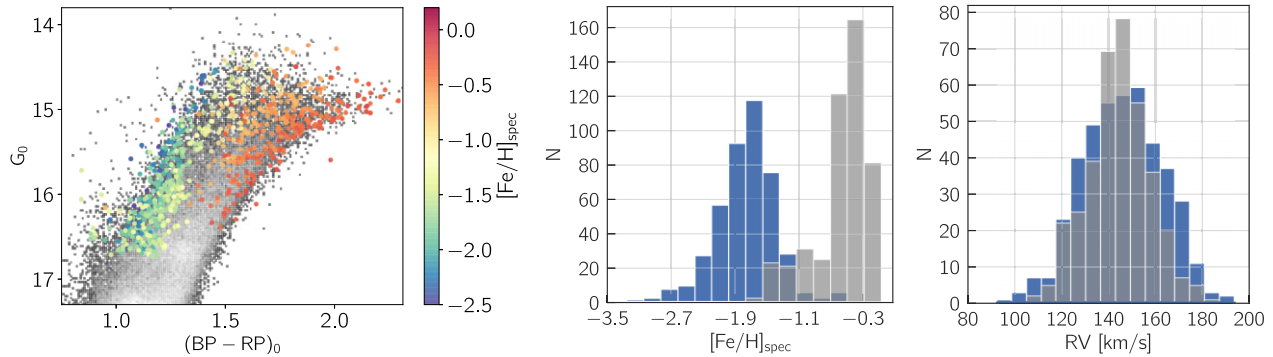


Figure 5. *Left:* Same CMD as in Fig. 4, plus the cross-match with APOGEE and the PIGS follow-up, colour-coded by their spectroscopic metallicities. *Middle:* spectroscopic metallicities from APOGEE DR16 (grey) and PIGS (blue) in our Sgr sample. *Right:* radial velocities from the same APOGEE and PIGS samples. The stars are well-distributed around 140 km s^{-1} , the mean Sgr radial velocity (Ibata et al. 1994).

following equations:

$$\begin{aligned} \overline{\mu_\alpha} &= -2.69 + 0.009\Delta\alpha - 0.002\Delta\delta - 0.00002\Delta\alpha^3 \\ \overline{\mu_\delta} &= -1.35 - 0.024\Delta\alpha - 0.019\Delta\delta - 0.00002\Delta\alpha^3 \end{aligned} \quad (1)$$

where $\Delta\alpha = \alpha - \alpha_0$, $\Delta\delta = \delta - \delta_0$ represent the difference in RA and Dec. with respect to the Sgr centre. We assume the nuclear globular cluster M54 (NGC 6715) to be at the Sgr centre, with coordinates $\alpha_0 = 283.764^\circ$ and $\delta_0 = -30.480^\circ$.

We present the colour–magnitude diagram (CMD) and the Pristine colour–colour diagram for the Sgr selection (after applying the cuts above) in Fig. 4. The Ca H&K term appears in the y-axis of the colour–colour diagram, making it sensitive to metallicity and creating a spread in the metallicity values along the vertical axis. One can see three distinct blobs in the colour–colour diagram. The largest blob consists of red giant branch (RGB) stars in Sgr.

The small blob of stars around $(BP - RP)_0 = 0.8$ and y-axis = 6.5 has values spreading a wide range in parallax compared to the rest of the stars. These are likely foreground stars, which we decide to cut using the red-dashed line in Fig. 4, together with all bluer stars that are mostly other types of contamination. With this last cut, our final Sgr sample contains 44 785 stars.

The stars in the distinct sequence in the colour–colour diagram between $\sim (BP - RP)_0 = 0.9\text{--}1.2$ (between the red- and blue-dashed lines) do not have a different parallax distribution compared to the main group of stars, and follow the spatial distribution of the main group of stars as well. We hypothesize that these are not foreground stars, nor Sgr RGB stars, but rather Sgr helium-burning red clump/horizontal branch stars, which have slightly higher temperatures compared to the normal red giants and hence form a distinct sequence in the colour–colour diagram. The main red clump in Sgr occurs at $G_0 \sim 17.7$ and it is excluded from our selection, hence the brighter red clump stars must be on the near side of the dwarf galaxy to enter in our $G_0 < 17.3$ selection.

2.3 Spectroscopic samples

We use spectroscopy from two different Sgr samples to evaluate to our Sgr selection. The first sample we use is APOGEE DR16 (Ahumada et al. 2020), with which we have 568 stars shared with our Sgr selection. Most of these are relatively MR ($[\text{Fe}/\text{H}] > -1.0$), see the middle panel of Fig. 5. We checked the latest APOGEE release as well (DR17; Abdurro’uf et al. 2022), but did not find any additional stars in common with our Sgr selection.

The second sample we use is a spectroscopic follow-up from PIGS, which contains almost exclusively lower metallicity stars. Arentsen et al. (2020) presented the PIGS low- and medium-resolution spectroscopic follow-up of MP inner Galaxy candidates, obtained with AAOmega + 2dF on the AAT (Lewis et al. 2002; Saunders et al. 2004; Sharp et al. 2006). The low-resolution ($R \sim 1300$) optical and intermediate resolution ($R \sim 11\,000$) calcium triplet spectra were analysed through a full-spectrum fitting using the FERRE code¹ (Allende Prieto et al. 2006), providing effective temperatures, surface gravities, metallicities, and carbon abundances (see Arentsen et al. 2020 for details). More spectroscopic follow-up was obtained later in 2020, which has been analysed in the same way and has already been used in Arentsen et al. (2021). In total, four AAT pointings included dedicated observations of Sgr stars (see their positions in Fig. 1). These have not yet been discussed in any publication.

The Sgr selection for the follow-up was made by adding two simple *Gaia* DR2 cuts to the PIGS selection: $(\varpi - \epsilon_\varpi) < 0.1$ and proper motions within 0.6 mas yr^{-1} of $\mu_\alpha = -2.7$ and $\mu_\delta = -1.35$ no transformations like equation 1 were applied. We used *Gaia* DR2 because the spectroscopic follow-up was done before *Gaia* EDR3, as part of the main PIGS follow-up program predating the current work. The Sgr selection was extended to half a magnitude deeper ($G = 17.0$) than the main PIGS sample. Whereas the PIGS fields were observed for 2 h each, two of the Sgr fields were observed for 3 h, one for 2.5 h and one for 1.5 h. The CMD and metallicities of PIGS stars in our final Sgr selection are shown in the left-hand and middle panels of Fig. 5. The cross-match between the PIGS AAT spectroscopy and our selected Sgr sample results in 426 objects (keeping only stars with good quality spectroscopic parameters, following Arentsen et al. 2020). Together, the APOGEE and PIGS samples cover the full metallicity range of Sgr.

We present the radial velocities from the spectroscopic PIGS and APOGEE stars in our Sgr sample in the right-hand panel of Fig. 5. For our selection, the median APOGEE and PIGS radial velocities are $\approx 144.5 \text{ km s}^{-1}$ and $\approx 145.6 \text{ km s}^{-1}$, respectively. The resulting histogram shows that the radial velocities have a smooth distribution with no clear outliers, around the mean literature Sgr radial velocity of $\sim 140 \text{ km s}^{-1}$ (Ibata et al. 1994). The PIGS sample has a slightly higher velocity dispersion than the APOGEE sample, which is in line with the expectation that MP stellar populations are typically older and more pressure-supported. We will further discuss this scenario in Section 4.

¹FERRE is available at <http://github.com/callendeprieto/ferre>

The colour-coding of CMD shown in the left-hand panel of Fig. 5 displays the spectroscopic metallicities of the PIGS and APOGEE stars. The most MP stars are located on the blue side, while the redder part is populated by cooler MP stars. From the metallicity histogram in the middle panel, the dominance of PIGS among the MP stars with respect to the APOGEE sample is clear, the result of PIGS being focused on the search of MP stars in Sgr. A comparison between metallicities from PIGS and APOGEE has been made for bulge stars in Arentsen et al. (2020), finding good agreement – a dispersion of 0.2 dex, and only a slight systematic offset (with APOGEE being more MR by 0.1–0.2 dex, depending on the metallicity).

2.4 Spectroscopic calibration sample

We make use of a training sample with available spectroscopic metallicities present in the footprint of the main *Pristine* halo survey (Starkenburg et al. 2017) to derive iso-metallicity lines for the *Pristine* colour-colour diagram, which we will use to calibrate the metallicity scale of our photometric PIGS-Sgr sample. The training sample consists of the main training sample for the *Pristine* survey, which has been carefully built to contain many very MP stars (from SEGUE/Yanny et al. 2009, LAMOST/Li, Tan & Zhao 2018 and the dedicated *Pristine* follow-up/Aguado et al. 2019), enriched with additional stars from APOGEE DR16 (Ahumada et al. 2020) to extend the training sample to higher metallicities and lower temperatures. Because we only have giant stars in our Sgr sample, we only keep the giants in the training sample ($\log g < 3.8$ and $T_{\text{eff}} < 5700$ K). After cross-matching this spectroscopic sample with the most recent internal *Pristine* *CaHK* catalogue (already cross-matched with *Gaia*), de-reddening it in the same way as our Sgr photometry and applying the same photometric quality cuts as before, we obtain a sample of $\sim 23\,000$ giant stars with $-4.0 < [\text{Fe}/\text{H}] < +0.5$. The resulting sample is shown on the *Pristine* *CaHK-Gaia* colour-colour diagram in the upper panel of Fig. 6, colour-coded by the spectroscopic metallicities from the training sample. On top of it, we show our derived iso-metallicity lines, ranging from -3.0 to 0.0 in steps of 0.5 dex, which will be further described in the following section.

3 METALLICITY ANALYSIS

The following section reports the metallicity analysis conducted on the photometric Sgr selection with the help of the spectroscopic training sample. With the aim of studying the distribution of different metallicity populations in Sgr, we divide the sample in two main groups and study their spatial distribution. We also fit models to the Sgr stellar density, paying attention to a possible metallicity gradient within Sgr. Finally, we present the spatial distribution of the very MP stars.

3.1 Derivation of iso-metallicity lines

We employ the spectroscopic training sample from the main *Pristine* survey to derive iso-metallicity lines in the *CaHK-Gaia* colour-colour space, which we will use in our Sgr analysis to divide the sample into various groups of metallicity. Some iso-metallicity lines have been derived for the *Pristine*-SDSS colour space before, but not for the *Pristine-Gaia* colour-colour space. For this work, we are only interested in giants since only giants are part of our Sgr selection. We binned the colour-colour space in $(\text{BP} - \text{RP})_0$ and selected slices of spectroscopic metallicities within 0.1 dex of a given $[\text{Fe}/\text{H}]$, with a minimum number of five stars per $(\text{BP} - \text{RP})_0$ bin. To derive an

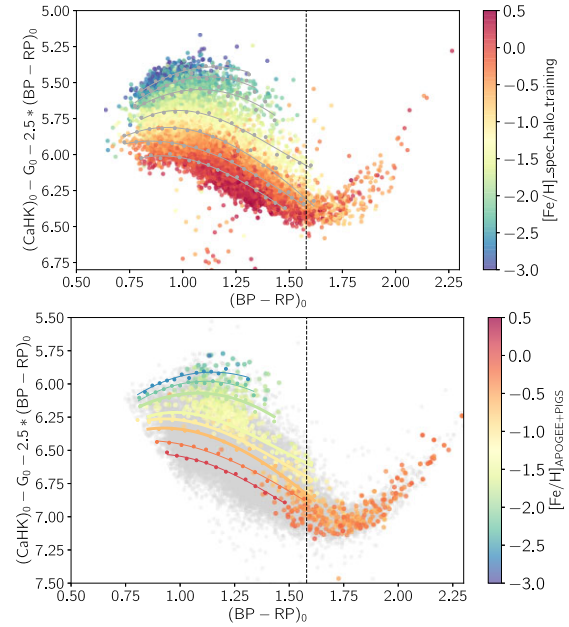


Figure 6. *Top:* colour-colour diagram for the main *Pristine* survey spectroscopic training sample, colour-coded by their spectroscopic metallicity. The grey lines are polynomials fitted through the grey points, which are medians of the binned $(\text{BP} - \text{RP})_0$ axis for stars within 0.1 dex of $[\text{Fe}/\text{H}] = -3.0, -2.5, -2.0, -1.5, -1.0, -0.5,$ and 0.0 , from top to bottom, respectively. *Bottom:* colour-colour diagram for our Sgr sample (full sample shown in grey), with the spectroscopic Sgr sample from APOGEE and PIGS colour-coded by their spectroscopic metallicity. Overplotted are the iso-metallicity lines derived from the training sample, after applying a vertical offset to match with the Sgr spectroscopic metallicities. The thicker lines mark the threshold values used to divide different metallicity populations in this work, namely $[\text{Fe}/\text{H}] = -2.0, -1.5, -1.3,$ and -1.0 . The vertical dashed lines at $(\text{BP} - \text{RP})_0 = 1.6$ in both panels limit the area for which we use the iso-metallicity lines (on the left). The stars redder than this will all be classified as MR based on the spectroscopic $[\text{Fe}/\text{H}]$ available.

iso-metallicity line, we determined the median y-axis value in each bin and successively fit a second-order polynomial to these points for $[\text{Fe}/\text{H}] \leq -1.8$ and a third order for $[\text{Fe}/\text{H}] \geq -1.7$. The resulting iso-metallicity lines are shown in the upper panel of Fig. 6, on top of the spectroscopic training sample from the main *Pristine* survey. The lines range from $[\text{Fe}/\text{H}] = -3.0$ to $[\text{Fe}/\text{H}] = 0.0$ dex, in steps of 0.5 dex. We limit the polynomials to $(\text{BP} - \text{RP})_0 < 1.6$, since for redder colours the MP and MR stars start overlapping and crossing.

The derived iso-metallicity lines are on the main survey calibration scale for the *CaHK* photometry, but the Sgr-PIGS photometry is on a different scale, offset by a constant. To determine the offset, we used the available Sgr spectroscopy from APOGEE and the PIGS/AAT data, which is shown and colour-coded by metallicity in the bottom panel of Fig. 6. We compute the offset between a given iso-metallicity line and the stars in the Sgr spectroscopic sample falling in the same metallicity range. We used Sgr stars with $-1.6 < [\text{Fe}/\text{H}] < -1.4$, $-1.9 < [\text{Fe}/\text{H}] < -1.7$, and $-2.1 < [\text{Fe}/\text{H}] < -1.9$, and computed the difference between these stars and the iso-metallicity lines at $[\text{Fe}/\text{H}] = -1.5, -1.8,$ and -2.0 , respectively, finding an average shift of 0.52 mag. In the bottom panel of Fig. 6, the same iso-metallicity lines from the upper panel (plus one at $[\text{Fe}/\text{H}] = -1.3$ represented by the thicker yellow line) are shown, now shifted with the offset derived above to match the Sgr

colour–colour space. They are colour-coded by the corresponding spectroscopic metallicity.

We found that the shift between the Sgr spectroscopic metallicities and the iso-metallicity lines derived from the training sample depends on the exact metallicity range that is used. We hypothesize that this is connected to a significant difference in the $[\alpha/\text{Fe}]$ abundances between MW stars and Sgr stars. In the training sample from the main *Pristine* survey, the reddest part of the colour–colour diagram (with $(\text{BP} - \text{RP})_0 \gtrsim 1.5$) splits into two sequences for giants when colour-coded by $[\alpha/\text{Fe}]$ from APOGEE. Their alpha abundances are representative of thin and thick disc stars. The Sgr $[\alpha/\text{Fe}]$ is significantly lower than both of those (Hasselquist et al. 2017). Some discussion on this can be found in the appendix. For this reason, we will not be determining individual photometric metallicities for each star in this paper, because it is not clear exactly what scale they would be on. The choice of cuts performed employing these iso-metallicity lines is extensively discussed in further sections, and we show that our main interpretations do not depend on the details.

3.2 Metallicity division for Sgr stellar populations

The iso-metallicity lines offer an effective way to separate the Sgr sample into two main populations, one MR and one MP population. Looking at how the choice of different iso-metallicity lines has an impact on the metallicity distribution within the Sgr core gives an insight about the role of the selection effect on the final results.

First, we use the iso-metallicity line at $[\text{Fe}/\text{H}] = -1.0$ dex (thicker orange line in Fig. 6). With this division, 14 670 stars compose the $[\text{Fe}/\text{H}] < -1.0$ group and 30 115 stars are identified with $[\text{Fe}/\text{H}] > -1.0$. Next, we test the separation using $[\text{Fe}/\text{H}] = -1.3$ (the line is coloured in yellow in Fig. 6), resulting in an MP population of 9719 stars and an MR population of 35 066 stars. Finally, we also tested a division at $[\text{Fe}/\text{H}] = -1.5$ (thicker light-green line), obtaining 6195 stars with $[\text{Fe}/\text{H}] < -1.5$ and 38 590 stars with $[\text{Fe}/\text{H}] > -1.5$. The polynomial division is valid until $(\text{BP} - \text{RP})_0 = 1.6$. Thanks to the APOGEE data set, it is possible to classify the stars sitting on the redder part of the diagram (on the right of the dashed line in Fig. 6) as all being part of the population with higher metallicity, as there are 305 spectroscopic stars with $(\text{BP} - \text{RP})_0 > 1.6$ with $[\text{Fe}/\text{H}] > -1.0$. We include the reddest stars in our MR populations in the remainder of this work.

3.3 Spatial distributions

Next, we build density maps of the MP and MR populations defined in Section 3.2 to study their spatial distributions. The spatial distributions are shown in the left and middle columns in Fig. 7 for the three different metallicity separations, all of which practically show the same pattern: a higher stellar density is found in the centre of Sgr around M54, while the number of observed stars drops moving outwards from the centre to the onset of the stream. One thing to notice is that the more MR component appears to be more centrally concentrated compared to the more spread-out MP population. The very central density of the two metallicity populations is dominated by the central globular cluster M54 (with average $[\text{Fe}/\text{H}] \simeq -1.55$, Carretta et al. 2010b). This relates to the very complicated metallicity distribution function of the central region of Sgr influenced by the presence of the nuclear star cluster (Bellazzini et al. 2008; Alfaro-Cuello et al. 2020).

We use Fig. 7 to investigate the presence of a metallicity gradient. The ratios between the MR and MP populations are shown in the right-hand column. The three rows correspond to different selections

obtained using iso-metallicity lines fitted for various metallicity values, i.e. $[\text{Fe}/\text{H}] = -1.5, -1.3$ and -1.0 . The histogram shows that the relative fraction of MP objects is higher further away from the centre, while the central area presents on average a lower fraction. This effect is less visible, although always present, as the metallicity limit for dividing the populations get lower. Indeed for the division at $[\text{Fe}/\text{H}] = -1.5$, the number of stars with $[\text{Fe}/\text{H}] > -1.5$ severely outnumber the MP counterpart and the values of their ratios are shifted towards much lower values.

For the analysis that follows in this work, we chose to use the stars with $[\text{Fe}/\text{H}] < -1.3$ as the MP populations, while for the MR group, we set $[\text{Fe}/\text{H}] > -1.0$. In this way, we ensure that the division between the two groups is more clean and not dominated by stars that are close to the dividing line. We check the photometric selection with the help of the APOGEE and PIGS spectroscopy available, which covers most of the investigated metallicity range. We find that ~ 98 per cent of spectroscopic stars with $[\text{Fe}/\text{H}] < -1.3$ are part of our MP population, while ~ 95 per cent of the stars with spectroscopic metallicities > -1.0 are part of our MR population. We have tested that this characteristic does not depend strongly on the metallicity limit used to separate the MP and MR components. The main result, that the MP/MR ratio increases further from the Sgr centre, is visible also when using even lower $[\text{Fe}/\text{H}]$ values for defining the MP population.

Fixing the limit for the MP population at $[\text{Fe}/\text{H}] = -1.3$ can also be justified by the estimated location of the alpha-knee in Sgr, although its position is still under debate as well as the corresponding $[\text{Fe}/\text{H}]$ value. It has been derived for M54 to occur at $[\text{Fe}/\text{H}] \sim -1.3/-1.4$ (Carretta et al. 2010a) and at $[\text{Fe}/\text{H}] \sim -1.3$ for the Sgr stellar streams (De Boer et al. 2014). The alpha knee is where the turnover happens in the $[\text{Fe}/\text{H}] - [\alpha/\text{Fe}]$ diagram, and is linked to the star formation rate of a system. Before this change in the $[\alpha/\text{Fe}]$ abundance, the chemical enrichment is mostly subjected to the presence of the supernovae type II from massive stars, which have much shorter time-scales than supernovae type Ia (SNIa) with lower mass progenitors. A galaxy that builds up and maintains metals and gas before SNIa start to contribute to the gas enrichment will reach a higher metallicity of the knee, compared to a galaxy that loses metals due to galactic winds, or does not show an efficient SFH (Helmi 2020).

3.4 Quantifying the differences between MP and MR populations

3.4.1 Method

To quantify the structural differences between the MP and MR populations, we fit a model to their spatial distributions. We bin the Sgr footprint in pixels of a few tens of arcmin, ~ 20 arcmin for the MP and ~ 15 arcmin MR, as the stellar density of this latter population is higher than the one of the MP component. We follow the approach of Martin, de Jong & Rix (2008) and express the Sgr stellar density as:

$$N_i = A_0 \exp^{-\frac{r_i}{r_e}} \quad (2)$$

where i indicates the pixel, A_0 is the central density, r_e is the exponential scale radius, and r_i is the elliptical distance of each pixel with respect to the centre of the distribution. The r depends on the ellipticity e and the position angle θ by:

$$r_i = \left(\frac{1}{1-e} (x_i \cos \theta - y_i \sin \theta)^2 + (x_i \sin \theta + y_i \cos \theta)^2 \right)^{1/2} \quad (3)$$

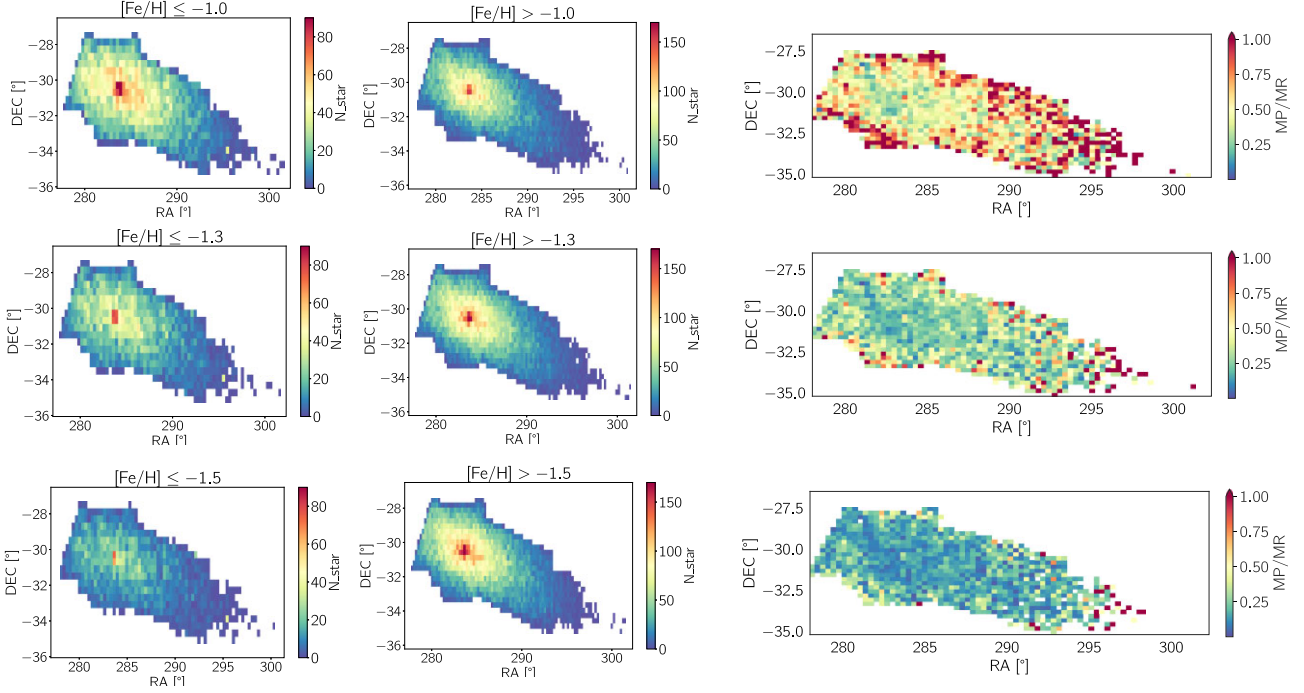


Figure 7. The first column represents the density distribution for the selected MP stars in equatorial coordinates. At the top, the MP group is derived using the $[\text{Fe}/\text{H}] = -1.0$ line, the middle plot is determined with the -1.3 metallicity line, while the selection at the bottom with $[\text{Fe}/\text{H}] = -1.5$. Similarly, the density maps for the various MR-selected populations ($[\text{Fe}/\text{H}] > -1.0$; $[\text{Fe}/\text{H}] > -1.3$; $[\text{Fe}/\text{H}] > -1.5$) are shown in the middle column. The right column displays the 2D histograms of the ratios between MP and MR stars (same selections adopted for the density maps) in RA and Dec. Each bin of 0.33° is colour-coded by the ratio value. To have a clear spread in the ratio range, the $\text{MP}/\text{MR} > 1$ are set to 1.

Where x_i and y_i are related to the RA (α) and Dec. (δ) and to the tangential plane of the sky by:

$$\begin{cases} x_i = \frac{\cos(\alpha_i) \sin(\alpha - \alpha_0)}{\cos(\delta_0) \cos(\delta) \cos(\alpha - \alpha_0) + \sin(\delta) \sin(\delta_0)} \\ y_i = \frac{\sin(\delta_0) \cos(\delta) \cos(\alpha - \alpha_0) - \cos(\delta_0) \sin(\delta)}{\cos(\delta_0) \cos(\delta) \cos(\alpha - \alpha_0) + \sin(\delta) \sin(\delta_0)} \end{cases} \quad (4)$$

with the centre at (α_0, δ_0) .

The best set of parameters were obtained using Markov Chain Monte Carlo sampling, using the EMCEE² package. We fit a model for the stellar density of the MP and MR populations, with the isometallicity lines at $[\text{Fe}/\text{H}] = -1.3$ and $[\text{Fe}/\text{H}] = -1.0$ as discriminant. The parameters used in the fit are reported in Fig. 8. For each fit, we used 64 walkers and 30 000 steps. We excluded all pixels more than 50 per cent outside of the PIGS-Sgr footprint (the black solid line in Fig. 9). The density of pixels with 50 per cent–100 per cent within the footprint has been scaled, according to the fraction inside the footprint. To not bias the fit due to the globular clusters in the footprint, we avoided pixels where M54 is located using a radius of 0.4° around the coordinates of the centre ($283.762^\circ, -30.479^\circ$; Harris 1996). For the MP population, we also removed the contribution of the two globular clusters Arp2 and Ter8 (Bellazzini et al. 2020), fixing the 2 centres at $(292.183^\circ, -30.356^\circ)$ and $(295.433^\circ, -33.999^\circ)$ and using a radius of 0.2° and 0.3° for Arp2 for Ter8, respectively.

We tested the inclusion of a Galactic background in the model, using an exponential function dependent on the Galactic latitude, but we found it to be unconstrained in the fitting procedure. This hints

at a very efficient cleaning of MW contamination in our member selection, which we further discuss in Section 4.

3.4.2 Results

The resulting parameters of our fits are summarized in Table 1 and Fig. 8, which gives the marginalized 2D posterior distributions of the set of parameters. Some correlation can be seen between α_0 versus δ_0 , re versus A , and re versus e , but the fitted parameters are overall well-constrained. Table 1 also reports the values for $[\text{Fe}/\text{H}] < -1.5$ and < -2.0 . For this last category, the pixel size is increased to ~ 30 arcmin and the lower number of stars is reflected in the uncertainties.

Fewer stars are included in the lower metallicity categories resulting in the decrease of the central density (A). We find that the scale radius (r_e) shifts significantly towards greater values for the lower metallicity populations. All other model parameters only show minor changes, which are likely not significant. We suspect that the uncertainties on the model parameters are underestimated, which we will briefly get back to in the discussion. The change of the position angle of ≈ 3.3 degrees between the MR and MP populations represents a change of only a small fraction, and similarly for the eccentricities.

The most visible difference between the centres of the main MP and MR populations concerns the RA component: $0.253_{-0.028}^{0.028}$ degree, but this is still only a small change that is unlikely to be significant. Our derived centres differ from the coordinates of M54 at maximum $\sim 0.31^\circ$ in RA for the MP stars, and $\sim 0.07^\circ$ for the MR population. Del Pino et al. (2021) derived the central coordinates of Sgr (excluding M54) to be $(\alpha, \delta) = (283.945^\circ, -30.647^\circ)$, which differs from our centres by $(\Delta\alpha, \Delta\delta) = (0.138^\circ, 0.172^\circ)$ for the MP and $(\Delta\alpha, \Delta\delta) = (0.115^\circ, 0.154^\circ)$ for the MR populations.

²<https://emcee.readthedocs.io/en/stable/>

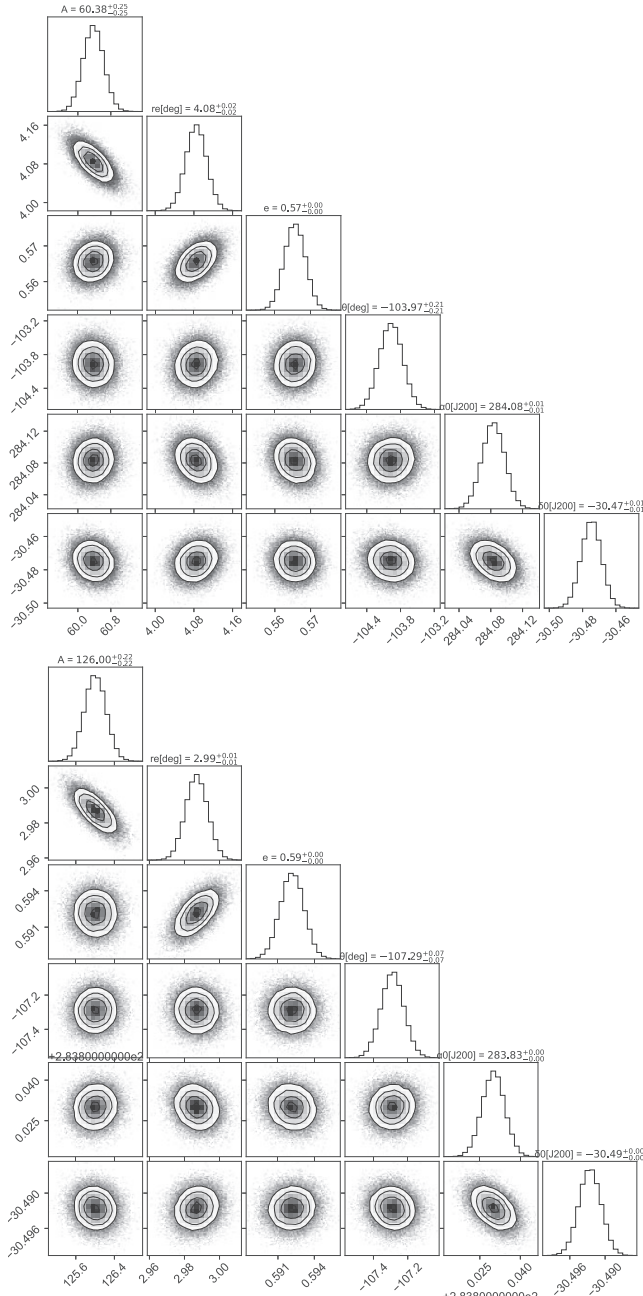


Figure 8. *Top:* corner plot illustrating the results of our model fit for the MP population ($[\text{Fe}/\text{H}] < -1.3$). They show the covariance between the set of parameters, hinting a correlation between r_e and A , r_e and e , and between the coordinates of the centre of the distribution (ra_0 , dec_0). *Bottom:* same, but for the Sgr MR population ($[\text{Fe}/\text{H}] > -1.0$).

The spatial distributions of the models and residuals are shown in Fig. 9. The residuals show structure for both the MP and MR fits, especially for the regions with $\text{RA} > 290^\circ$. Our elliptical model appears to be too simplistic to describe the distribution of stars in Sgr, which is not surprising given the complex, disrupting nature of the system. We do not expect the residuals to be related to the *Gaia* scanning law. The effect of the scanning law is strongest for faint stars (closer to the magnitude limit in *Gaia*, $G \gtrsim 20$), producing inhomogeneities on the scale of ~ 1 degree (Fabricius et al. 2021). In

Table 1. Structural parameters for different metallicity populations derived through our χ^2 minimization.

MP ($[\text{Fe}/\text{H}] < -1.3$)		
α_0 (J2000)	δ_0 (J2000)	A_0
$284.083^{+0.014}_{-0.014}$	$-30.475^{+0.006}_{-0.006}$	$60.375^{+0.250}_{-0.247}$
r_e (degree)	e	θ (degree)
$4.085^{+0.022}_{-0.021}$	$0.566^{+0.003}_{-0.003}$	$-103.971^{+0.208}_{-0.206}$
MR ($[\text{Fe}/\text{H}] > -1.0$)		
α_0 (J2000)	δ_0 (J2000)	A_0
$283.830^{+0.004}_{-0.004}$	$-30.493^{+0.002}_{-0.002}$	$126.008^{+0.222}_{-0.225}$
r_e (degree)	e	θ (degree)
$2.987^{+0.006}_{-0.006}$	$0.592^{+0.001}_{-0.001}$	$-107.289^{+0.067}_{-0.068}$
[Fe/H] < -1.5		
α_0 (J2000)	δ_0 (J2000)	A_0
$284.060^{+0.024}_{-0.024}$	$-30.483^{+0.011}_{-0.010}$	$30.601^{+0.226}_{-0.225}$
r_e (degree)	e	θ (degree)
$3.928^{+0.037}_{-0.036}$	$0.566^{+0.005}_{-0.005}$	$-103.955^{+0.359}_{-0.361}$
Very MP [$[\text{Fe}/\text{H}] < -2.0$]		
α_0 (J2000)	δ_0 (J2000)	A_0
$283.815^{+0.111}_{-0.111}$	$-30.396^{+0.058}_{-0.053}$	$9.722^{+0.306}_{-0.300}$
r_e (degree)	e	θ (degree)
$4.400^{+0.185}_{-0.173}$	$0.551^{+0.022}_{-0.023}$	$-104.506^{+1.704}_{-1.762}$

this work, we only use relatively bright stars ($G_0 < 17.3$) and do not make any strong cuts on any of the *Gaia* uncertainties.

3.5 Very metal-poor stars

The study of iron-depleted stars is of great interest for reconstructing the history of the Sgr galaxy, as they carry essential information to draw the story line of the early evolution of their host galaxy. Different investigations of VMP stars in Sgr over the years have led to an improved understanding of the early evolution of this dissolving system (Bellazzini et al. 2008; Hansen et al. 2018; Chiti & Frebel 2019; Chiti et al. 2020), but these are based on just a handful of known very MP stars. The blue, MP region of the Sgr CMD overlaps with the giant branch of the Galactic bulge, and before the *Gaia* data became available, it was difficult to disentangle these. Chiti & Frebel (2019) and Chiti et al. (2020) used the *Gaia* data in combination with narrow-band SkyMapper v photometry to identify 22 MP stars ($-3.10 < [\text{Fe}/\text{H}] < -1.45$) in Sgr, which was successful but still resulted in only a small sample.

The spectroscopic Sgr-PIGS follow-up sample contains 100 stars with $[\text{Fe}/\text{H}]_{\text{spec}} < -2.0$, which is the largest spectroscopic VMP Sgr sample to date. Our full photometric Sgr-PIGS data is an excellent source for more VMP stars. We selected VMP stars following the same approach explained in Section 3.2, but this time using the iso-metallicity line at $[\text{Fe}/\text{H}] = -2.0$ (see blue line in Fig. 6). Our VMP sample consists of 1150 stars, which is the largest sample of VMP candidates with $[\text{Fe}/\text{H}] < -2.0$ in Sgr to date.

The distribution of the VMP stars is shown in Fig. 10. Almost the entire selection (> 99.9 per cent) is far beyond the tidal radius of M54 (7.5 arcmin), therefore not associated to the globular cluster (Harris 2010). It is clear that these ancient stars are located at all radii but do follow the overall Sgr density distribution, the stellar density being higher in the centre. Around $\text{RA} \sim 295^\circ$, an over-density of

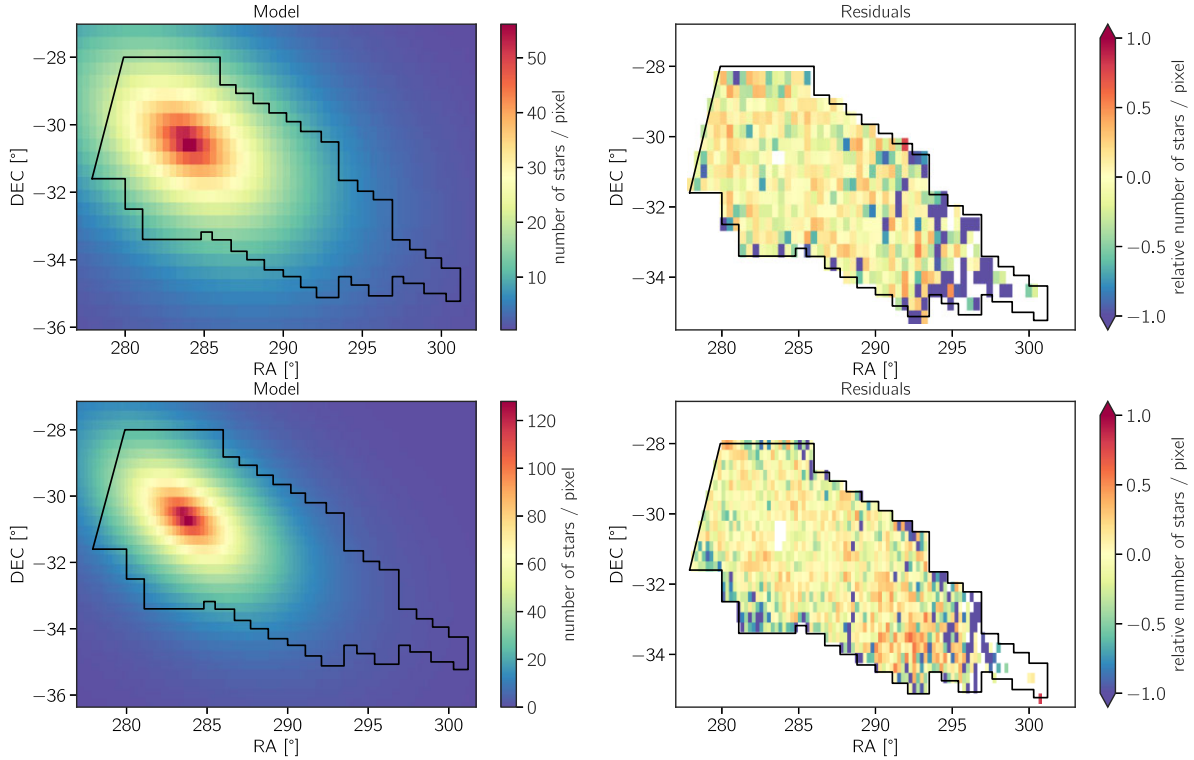


Figure 9. *Left:* our best models for the MP population ($[\text{Fe}/\text{H}] < -1.3$, top) and MR population ($[\text{Fe}/\text{H}] > -1.0$, bottom), colour-coded by the number of stars. The PIGS Sgr footprint indicated by a black solid line. *Right:* residuals of the fits in relative scale (difference between the data and the model divided by the number of stars in each pixel). The colour bar is restricted between -1 and $+1$ for a clearer visualization of their distribution along the footprint. The corresponding observed data are shown in the panels of Fig. 7.

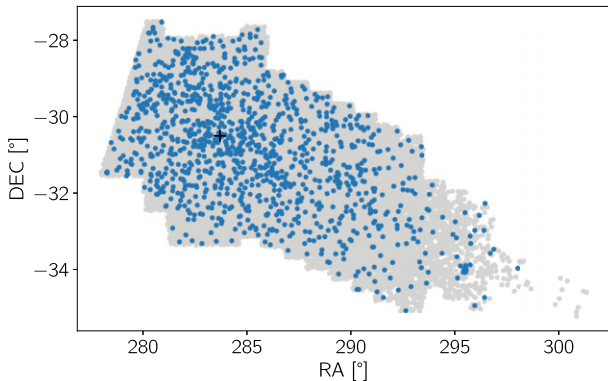


Figure 10. Our selected sample of 1150 VMP stars (in blue) on top of the full Sgr sample shown in grey. The VMP stars are extended relatively uniformly over the dwarf galaxy, with a higher density around the centre of Sgr (M54 is indicated with a black cross).

stars is noticeable, which corresponds to the GC Ter 8 (which has a spectroscopic $[\text{Fe}/\text{H}] = -2.3$, Sollima et al. 2014).

3.6 Metallicity gradient

Many studies (e.g. Keller, Yong & Da Costa 2010; Hyde et al. 2015; Mucciarelli et al. 2017; Hayes et al. 2020; Garro et al. 2021) have shown that a metallicity gradient is present both in the streams and in a small central region of the Sgr remnant, which is connected to the intricate chemo-dynamical evolution of this dwarf galaxy. The PIGS data are an excellent data set to study the metallicity

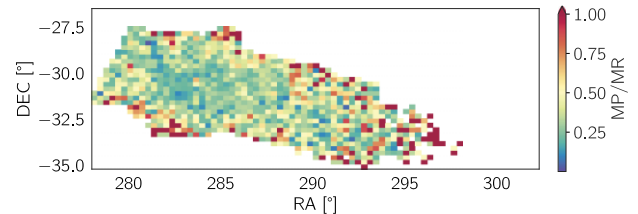


Figure 11. 2D histogram of the ratio between our final selected MP ($[\text{Fe}/\text{H}] < -1.3$) and MR ($[\text{Fe}/\text{H}] > -1.0$) populations. The binning and the colour-coding are same as the ones of Fig. 7.

gradient in the core of the galaxy. In Fig. 11, we show the same 2D histogram as in Fig. 7, this time with our MP ($[\text{Fe}/\text{H}] < -1.3$) and MR ($[\text{Fe}/\text{H}] > -1.0$) populations from the previous section, showing again the MP stars dominating at the edges and the MR in the central region.

Inspired by the idea of Mucciarelli et al. (2017) who mapped the change of metallicity as a function of the projected distance from the Sgr centre, we divide Sgr in concentric ellipses to examine the MP/MR ratio for each section, see Fig. 12. The ellipses are built using the parameters that we derived for the MR population in Section 3.4, which appear in Table 1. The ellipses have a fixed width of 1.2 degree along the semimajor axis, except for the innermost region, where we chose smaller ellipses to probe the effect of M54 (with each bin containing at least 300 stars), and for the two outermost bins, where the density of Sgr stars drops rapidly. The area covered is significantly larger compared to the one considered by Mucciarelli et al. (2017), as we computed the ratio out to $\sim 12^\circ$ from the position of M54 along the Sgr semimajor axis, whereas the previous analysis only

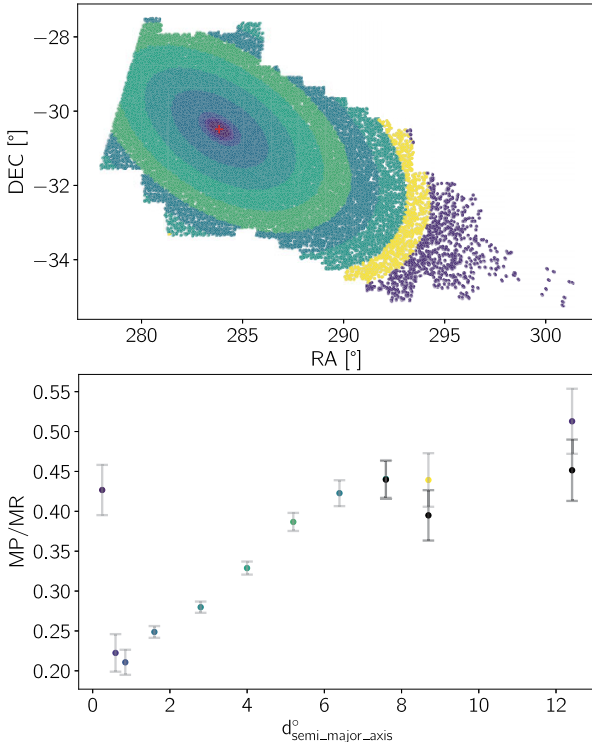


Figure 12. *Top:* division of our Sgr sample in concentric ellipses. The parametrization of each ellipse is defined using the fitted parameters from the MR population (see Table 1). The centre of each ellipse is represented by the red cross ($283.830^\circ; -30.493^\circ$). *Bottom:* the ratios of MP/MR stars in each ellipse. The error bars are calculated assuming a Poissonian distribution and the colours of the points correspond to the colours in the top panel. The distances on the x-axis are calculated along the semimajor axis of each ellipse with respect to the centre, taking the middle distance between two consecutive ellipses. For the outer three ellipses, the black points represent the ratios after removing the globular clusters Arp2 and Ter8.

went out to $\sim 0.15^\circ$ (or 9 arcmin). Similarly, the number of targets investigated is greatly increased with respect to the spectroscopic sample of Mucciarelli et al. (2017), which accounted for 235 stars.

By computing the ratio MP/MR for each division, as shown in Fig. 12, it is possible to appreciate the change of the metallicity moving away from the centre. The distances are set along the semimajor axis of each ring with respect to the centre of the MR population (with $[\text{Fe}/\text{H}] > -1.0$, see Table 1) using the projected coordinates from equation 4. The error bars are calculated assuming a Poissonian distribution. We find that Sagittarius presents a clear negative metallicity gradient – the relative number of MP stars is higher at larger radii from the centre of the galaxy.

For the central ellipse, the stellar budget of M54 contributes by enhancing the relative number of MP stars. The last rings, located furthest away from the centre of the galaxy, have higher uncertainties due to the lower stellar density in the outer Sgr region. The outer two ellipses also contain the two MP globular clusters Ter8 and Arp2, with $[\text{Fe}/\text{H}] \sim -2.37$ and $[\text{Fe}/\text{H}] \sim -1.77$ (Mottini, Wallerstein & McWilliam 2008), at $(\alpha, \delta) \approx (292^\circ, -34^\circ)$ and $(\alpha, \delta) \approx (292^\circ, -30^\circ)$; Goldsbury et al. 2010), respectively. For the outer three ellipses, the black points illustrate the MP/MR ratios after removing the stellar contribution from these two clusters. Excluding these two systems, we find that the trend seems to flatten starting at $d \sim 8^\circ$.

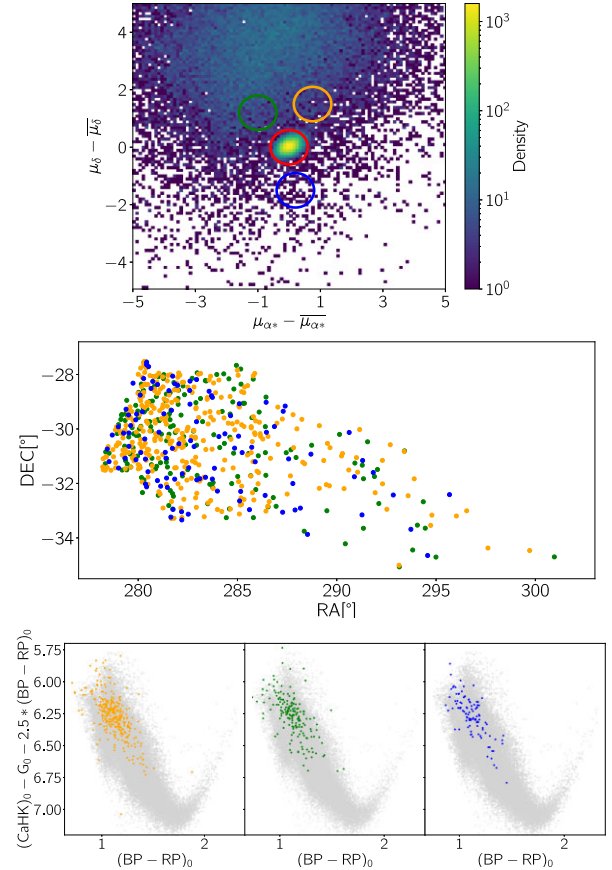


Figure 13. *Top:* PM distribution of stars in our Sgr sample before making a proper motion cut (the same as in Fig. 3), with our selected Sgr sample in red, and three other indicated regions as MW control fields. *Middle:* RA/Dec distribution of the stars from the control regions, in corresponding colours to the circles above. *Bottom:* colour-colour diagrams of our final Sgr selection (grey) and the stars in the control regions on top, again in the same colour coding.

4 DISCUSSION

4.1 Sources of uncertainties

Our analysis is subject to uncertainties, which we discuss below. Overall, they do not significantly affect our main conclusions.

4.1.1 MW contamination

Despite the numerous cuts applied, some MW foreground (or background) stars could still remain in the Sgr sample. We tested the level of contamination by selecting some MW control regions in different parts of the proper motion space, to check their numbers and to see how they are distributed in the footprint and the colour-colour diagrams. We apply exactly the same cuts as to our Sgr sample, except for the proper motions. We selected three circular regions with the same PM radius as for our Sgr selection in roughly the same region of the PM space, which are shown in orange, green, and blue circle in Fig. 13. Two of these fields, the green and orange circles, have higher densities than we expect in the Sgr region and show a pessimistic case of what the contamination level could be (175 and 332 stars). The control field depicted in blue contains even fewer stars (only 100). These numbers are to be compared with the 44 785 stars in our Sgr selection. From the numbers of stars in each control region, it is possible to compute

the percentage of the possible level of contamination left, which reaches at maximum ≈ 0.4 per cent, 0.7 per cent and 0.2 per cent for each field, respectively.

We show their distribution in RA and Dec. in the middle panel of Fig. 13. The stars are mostly concentrated closer to the Galactic plane (on the left), and their density fades away towards higher RA (further away from the plane). The low ratio of MW stars left in the outer part of Sgr indicates that the contribution from the MP MW halo is not dominant and it should not affect our metallicity analysis in the lower density regions.

We inspected the location of the control fields in the colour–colour diagram (bottom panels) and found out that they are mostly located in the bluer part of the diagram, overlapping with the region that we identified as Sgr red clump stars. The contamination appears to be split between the MR and MP groups in roughly equal proportions compared to the Sgr stars, therefore they should not bias the results from our metallicity analysis. We tested whether it made a difference to our main results to exclude the RC region of the colour–colour diagram in our Sgr selection (using the blue line in Fig. 4). We found no large differences, and therefore decided to keep the red clump region in our analysis.

As described in Section 3.4, we considered the MW contribution in the model fitting and found that it was unconstrained and did not impact the main results. This is consistent with our estimate of the MW contamination in this section, finding that it is very small.

4.1.2 Brightness cut

The choice of the magnitude cut ($G_0 = 17.3$), which noticeably reduced the Sgr sample (80 per cent of the original sample within the available magnitude range), has the advantage to give us a clean sample in the sense that the astrometry and the photometry are better constrained, enabling a more effective cleaning from the MW foreground stars. Whilst fainter targets might be interesting to have a more stars of this galaxy, we decided to reject the horizontal branch and the red clump region because it would make the selection of MR and MP populations more complicated and less complete. Furthermore, discarding the horizontal branch means to remove variable stars, which start appearing in this region of the diagram.

4.1.3 Iso-metallicity lines

For the derivation of the iso-metallicity lines, we considered using the *CaHK* and *Gaia* G, BP, and RP uncertainties. The uncertainties in *CaHK* are all < 0.08 , and when included in the fitting operations, our results did not change significantly. The errors on the *Gaia* photometry are much smaller than the *CaHK*, hence we ignored them as well. As mentioned earlier in the text (Section 3.1), the iso-metallicity lines stop to be trustworthy for the coolest stars, namely $(BP - RP)_0 > 1.6$, because in this region the MP and MR sequences start crossing each other. For this reason, we relied on the APOGEE [Fe/H] values to classify stars with $(BP - RP)_0 > 1.6$ as all being MR. We also found that in the spectroscopic training sample, the location of stars in the *Pristine* colour–colour diagram depends on the alpha abundances for the coolest/reddest stars (with $(BP - RP)_0 > 1.5$), resulting in a degeneracy between metallicities and alpha abundances. The alpha abundances in Sgr are different compared to those in the MW, therefore the iso-metallicity lines derived from the training sample could be partly inappropriate for Sgr. This may be connected to our finding that the *CaHK* shift

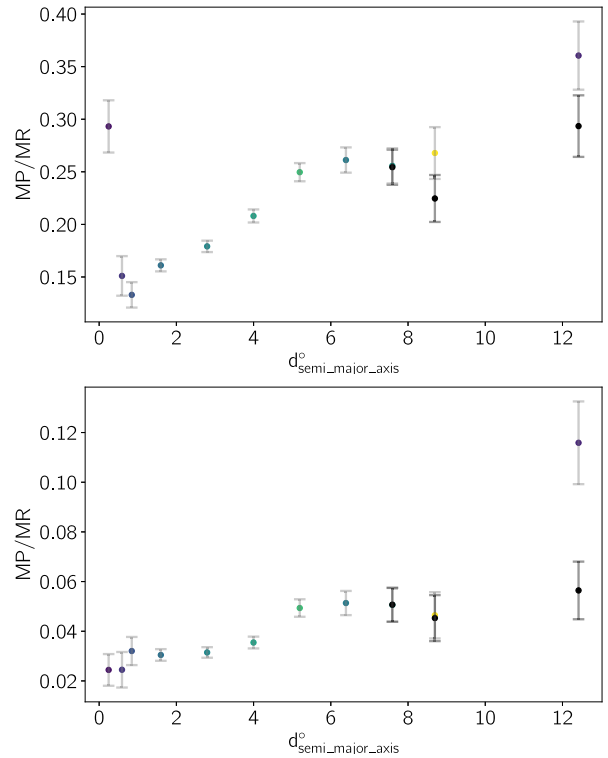


Figure 14. Same MP/MR ratio as in the bottom panel of Fig. 12, but presenting populations selected with different photometric metallicity thresholds for the MP population (top: $[\text{Fe}/\text{H}] < -1.5$, bottom: < -2.0). The MR group is always defined as $[\text{Fe}/\text{H}] > -1.0$.

between the spectroscopic training sample and the Sgr spectroscopy sample appears to depend on the metallicity of the Sgr stars used.

It is worth mentioning that the iso-metallicity lines were derived from a sample with low extinction towards the Galactic halo, whereas the Sgr region presents higher extinction since it is relatively close to the Galactic disc. Uncertainties in the extinction correction mean that this difference is expected to slightly increase the uncertainties in the metallicities for the Sgr sample, but it is not expected not create a systematic offset in the metallicity calibration.

4.1.4 Definitions of MP and MR populations

Figs 7 and 11 showed that, even when shifting the metallicity boundary for the MP and MR regions between -1.0 , -1.3 , -1.5 , and -2.0 , the fraction of MP stars relative to the MR ones always increases with distance from the centre of Sgr, therefore the metallicity gradient remains and does not depend on our exact definition of the MP population. This effect was quantified in the bottom panel of Fig. 12 for our main MP ($[\text{Fe}/\text{H}] < -1.3$) and MR ($[\text{Fe}/\text{H}] > -1.0$) populations, presenting a clear negative metallicity gradient. Choosing the two more MP boundaries introduced in Section 3.2 ($[\text{Fe}/\text{H}] < -1.5$ and < -2.0) for the MP population instead, we reproduce a similar trend of the MP/MR ratio rising away from the centre for these cases, presented in Fig. 14. In both panels, it is possible to notice a flattening in the trend starting at around $d \sim 6^\circ$. The fraction of stars with $[\text{Fe}/\text{H}] < -1.5$ appears to be relatively constant in the outermost rings, except for the last annulus. In this last ring, the ratios of MP and MR stars experience an important rise due to the presence of Arp2 and Ter8 that lay in this same region. From the same figures, it can be observed that the

flattening is stronger when the contribution from the two MP clusters, Arp2 and Ter8, is removed. For the $[\text{Fe}/\text{H}] < -2.0$ stars, there is no sign of M54 in the innermost rings anymore, and the rest of the trend shows a similar flattening as the previous case.

It is beyond the scope of this paper to further quantify the gradient (e.g. in terms of dex/kpc), which requires individual metallicity estimates for all our stars. For that, a larger spectroscopic sample of Sgr stars is needed, either to be used by itself or to better constrain the photometric metallicities.

4.1.5 Model fitting

The exponential elliptical profile adopted in our model fitting is a relatively simple approximation. Although it roughly corresponds to the projected shape of Sgr, the real distribution of Sgr stars is more complex. The model fits may also be influenced by inhomogeneities throughout the footprint. Both could result in unrealistic uncertainties from the Markov chain Monte Carlo (MCMC). We checked whether the results from the model fits depend on the binning of the data and find no significant changes.

To investigate whether differences for the model parameters between the MP and MR populations are likely to be real, we performed model fits on Sgr stellar populations in smaller metallicity bins (0.2 dex wide). We found a trend with metallicity for the scale radius, but found no clear evidence of trends with metallicity for the eccentricity, position angle, and centre of the models. We also concluded from this exercise that the uncertainties from the MCMC appear to be underestimated. In view of these considerations, the changes between the different model parameters (see Table 1), except for the scale radius, should be treated with caution.

4.2 Sgr metallicity gradient compared to the literature

Evidence of a metallicity gradient in Sgr was already reported early on Bellazzini, Ferraro & Buonanno (1999a). Those authors connected the presence of a metallicity gradient to a significant age variation in the dwarf system, caused by a protracted SFH. Alard (2001) studied two Sgr fields of $2 \times 2^\circ$, discovering a variation of -0.2 dex along the Sgr major axis that was linked to an age variation inside the core.

Thanks to near-infrared photometry, McDonald et al. (2013) studied the variation of the fraction of MP ($-1.6 < [\text{Fe}/\text{H}] < -0.9$) and intermediate, MR ($[\text{Fe}/\text{H}] > -0.7$) stars in an area of 11 square degrees and revealed that the MP population is more spread throughout the dSph, while the MR stars ($[\text{Fe}/\text{H}] \sim 0.0$) are grouped in ellipsoidal distribution around the centre of the galaxy. McDonald et al. (2013) identified clear traces of a metallicity gradient away from the region dominated by the bulge population (from $\text{RA} \sim 287^\circ$). Mucciarelli et al. (2017), through their spectroscopic study of 235 stars in the Sgr core and in M54 (all within 9 arcmin of the centre), uncovered a metallicity gradient as well, finding a higher fraction of MR stars in the centre. They speculated that the metallicity gradient in that region can be linked to an extended SFH, in which recent MR bursts took place in the central area of Sgr, which might have caused later stellar generations to be more centrally concentrated.

Our results are consistent with previous works, namely our MR population ($[\text{Fe}/\text{H}] > -1.0$) dominates the innermost region while our MP population ($[\text{Fe}/\text{H}] < -1.3$) becomes more important at larger radii, i.e. there is a metallicity gradient in our data. In line with these results, the greater value of the scale radius for the more MP stars could be an indication that, generally, the stars belonging to this

category are more smoothly distributed on larger distances compared to the more centrally concentrated MR stars. By comparing the r_e values derived for a number of populations in narrower metallicity bins, we found a clear increase of this parameter moving to lower metallicities.

We note that our work covers an area of ~ 100 square degrees, extending to ~ 12 degrees from the very centre of the galaxy, which is considerably larger than the region covered in previous studies, which typically focused on the very inner part of Sgr. Here, we find that the metallicity gradient of Sgr extends beyond the central part of the galaxy, and it manifests all the way outwards to the stream. The Sgr streams have metallicity distributions peaking at lower metallicity values than its core, $[\text{Fe}/\text{H}] \approx -0.8/ -1.1$ and $[\text{Fe}/\text{H}] \approx -0.5$, respectively (Hayes et al. 2020). Our analysis revealing a higher fraction of stars with $[\text{Fe}/\text{H}] < -1.3$ in the outskirts ($\text{RA} > 290^\circ$) is in congruence with these findings, supporting the scenario in which the most MP stars were the least bound to Sgr, and have been tidally stripped away from the core first.

This result highlights the power of the *Pristine* data, which enables us to characterize not only the dense central regions of the dwarf galaxy but also the outskirts. Combined with *Gaia* astrometric information, the photometric metallicity information is ideal to study the structural properties of a dwarf system along its entire extension.

4.3 The formation and evolution of Sgr

At this stage of the work, it is tantalizing to tie the results from our metallicity analysis to the history and evolution of Sgr. In general, the morphology and the SFH of a system can be heavily influenced by various physical processes that can be both internal, such as feedback from SNe events and gas pressure support, or triggered by external factors, e.g. ram pressure stripping and tidal disturbances caused by Galactic tides (tidal stripping and tidal stirring; Mayer et al. 2001, 2006; Łokas et al. 2010) or mergers (Starkenburg & Helmi 2015; Benítez-Llambay et al. 2016).

Recently, Tepper-García & Bland-Hawthorn (2018) and Vasiliev & Belokurov (2020) in their simulations assumed Sgr to have been a gas-bearing dwarf spheroidal galaxy before it fell into the MW. According to this theory, Sgr has conserved its origin of dSph despite the tidal interaction with the MW, and is predicted to dissolve over the next Gyr (Vasiliev & Belokurov 2020). Others suggest that the Sgr progenitor was a gas-rich, flattened rotating system that transformed into a dSph due to tidal stirring in the interaction with the MW, and whose inner core might survive the next pericentre passage (Łokas et al. 2010; Peñarrubia et al. 2010; Del Pino et al. 2021). Łokas et al. (2010) suggested that the Sgr progenitor resembled the Large Magellanic Cloud and they described it as a disc galaxy whose stellar populations formed a bar-like structure that survived until the second pericentre passage. The simulations of Oria et al. (2022) suggest that Sgr hosted a rotating component that has been perturbed during the interaction with the MW, but that this component was not the dominant fraction of the stellar mass. There is no consensus yet on the progenitor of Sgr, but more data might help to reach a conclusion. The arguments about the nature of the Sgr progenitor and its subsequent evolution are mainly based on the kinematical properties of Sgr and its stream, but there is another dimension as well: the chemistry.

4.3.1 Processes shaping the metallicity gradient

One process that is known to shape the age/metallicity gradients in satellite galaxies is ram-pressure stripping, which is responsible for removing the gas that was originally in the dwarf galaxy (Mayer

et al. 2001, 2006). Ram-pressure stripping first removes the gas in the less dense outer regions of a dwarf galaxy and the central gas reservoir at the very end. This means that new stars could be forming for longer periods of time in the centre compared to the outer regions. The gas in the inner regions is chemically enriched due to the prolonged star formation, hence this process can lead to age and metallicity gradients. We know that the Sgr core contains a population of relatively young stars (<2 Gyr, e.g. Siegel et al. 2007), so it must still have had gas up to those times. However, no gas has currently been detected in Sgr (Koribalski, Johnston & Otrupcek 1994; Burton & Lockman 1999). According to the modelling of Tepper-García & Bland-Hawthorn (2018), 30–50 per cent of the gas in Sgr was stripped ~ 2.7 Gyr ago (the first time it crossed the Galactic disc), while the complete loss of the remaining gas took place ~ 1 Gyr ago, when it crossed the disc the last time. Another process related to metallicity gradients in satellite galaxies is tidal stripping due to interaction with the host galaxy. Tidal stripping affects the more diffuse component of a dwarf more strongly, because it is less tightly bound to the galaxy. In Sgr, tidal stripping has led to the removal of much of its stellar content, which is now forming the large Sgr stream. The Sgr streams are more MP than the progenitor. The metallicities of their stellar populations span between $[\text{Fe}/\text{H}] \sim -2.5$ and ~ -0.5 (De Boer, Belokurov & Koposov 2015). This indicates that the MP stars were the ones that were less bound to the core, suggesting a radial metallicity gradient in Sgr. We also found in this work, using the radial-velocities available from the spectroscopic catalogues, that the velocity dispersion in the core of Sgr is higher for MP stars than for MR stars, supporting this scenario.

It has been shown that there is a difference between the metallicity gradient detected in dSph and dwarf irregular galaxies. Dwarf irregular galaxies (dIrrs) are rotationally supported and have a discy dwarf progenitor, while dwarf spheroidals are recognized to be pressure supported systems. Generally, the first category shows a steeper decreasing gradient profile with respect to the flatter trend present in dSph systems (Mayer et al. 2001; Taibi et al. 2022). Since the progenitor of Sgr is still under debate, we can expect that depending on the assumed scenario for the progenitor – a dSph or discy rotating system – the metallicity gradient would be less or more pronounced. It is also necessary to bear in mind that the transition from a disc galaxy to a dSph can be caused by the tidal stirring process, which has been invoked in the case of Sgr for being responsible for its observed elliptical shape (Łokas et al. 2010).

4.3.2 Connecting ages and metallicities

The relation between metallicity and age gradients is important in constraining the processes behind the metallicity gradient. Many works showed that age–metallicity relations can be derived for RGB stars in dwarf galaxies using information from their SFHs and CMDs (Carrera et al. 2011; del Pino, Aparicio & Hidalgo 2015; del Pino et al. 2017). However, these strategies are effective when the SFH concerns the same region of interest of the stars. We did not directly associate the metallicity gradient in our work with a possible age gradient, as it would have been beyond the scope of this paper. We could assume age–metallicity relations for Sgr from other works (see for instance Layden & Sarajedini 2000; Bellazzini et al. 2006; Siegel et al. 2007), but this is not trivial as most of them analyse fields of only a few degrees in the very central part around M54. Keeping that caveat in mind, if we adopt the age–metallicity relation presented by Siegel et al. (2007), we can speculate that our identified MR and MP populations have ages of ~ 4 – 8 and $\gtrsim 10$ Gyr, respectively.

Another way to connect ages and metallicities is by using their alpha abundances. The knee in the $[\text{Fe}/\text{H}] - [\alpha/\text{Fe}]$ diagram indicates the switch from star formation on shorter time-scales, where the SN type II were the main contributors to the gas enrichment, to star formation on longer time-scales, during which the metal enrichment from SN type Ia started to contribute significantly. The knee in the $[\text{Fe}/\text{H}] - [\alpha/\text{Fe}]$ diagram in M54 and the Sgr stream has been derived to be located at $[\text{Fe}/\text{H}] \sim -1.3$ (Carretta et al. 2010a; De Boer et al. 2014), and has been connected to an age of ≈ 11 Gyr. The knee is still somewhat unconstrained in the core and could be different, since the data suggest it experienced a prolonged and complex SFH. However, assuming it is around the same metallicity, this is another indication that our MP population is significantly older than the MR population.

Sgr has interacted with the MW for $\gtrsim 8$ Gyr, and the first close pericentre passage of Sgr is predicted to have happened ~ 5 – 6.5 Gyr ago (Law & Majewski 2010; Ruiz-Lara et al. 2020). Given an age of ~ 4 – 8 Gyr for the MR stars, this means that the younger MR stars might have been born during the first encounter as a consequence of the infalling triggered by the tidal interaction. Also the older MR stars and the MP stars would already be present at the time of the first interaction. However, we can not exclude that these populations will have been affected differently by the tidal interaction with the MW, depending on their internal properties at the moment of infall – i.e. how tightly they were bound to the remnant, and whether they had any rotation or not.

4.3.3 Metallicity gradient and its interpretation in Sgr

The processes playing a role in the formation of metallicity gradients in low-mass dwarf systems ($M_* \lesssim 10^8 - 10^{10} M_\odot$) remain not fully understood. There is not a clear consensus whether metallicity gradients are formed by protracted central star formation episodes with respect the outer regions, or if they are driven by processes acting more on the older, more MP stars by moving them outwards (Revaz & Jablonka 2018; Taibi et al. 2022), and/or a combination of these.

The complex combination of internal (such as rotation, orbits and angular momentum content) and environmental factors (tidal and ram-pressure stripping) plays a role in shaping and weakening metallicity gradients, and it is difficult to disentangle these additional factors from the role of an extended SFH (Mayer et al. 2006; Sales, Helmi & Battaglia 2010; Taibi et al. 2022) and consequently link the gradient to a progenitor.

By looking at our figures illustrating the various [MP/MR] ratios, the fact that it is still possible to detect a gradient might be interpreted as a hint of discy progenitor in which the gradient should have been strong enough to be partially preserve until today. The change of steepness observable at $\text{RA} \sim 290^\circ$ might be related to the transition from the outer core to the stellar stream, which might mitigate the profile observed for the very inner part where the various star formation bursts took place.

The work of Mercado et al. (2021) reported that a late gas accretion is a further event that can weaken or flatten an existing metallicity gradient in a dwarf galaxy. If we consider that Sgr might have experienced a first encounter with the MW around 5–6 Gyr ago, this factor should be added to the secular processes that act in weakening the trace of the original gradient. If we add to this picture the protracted SFH in Sgr, according to Benítez-Llambay et al. (2016), a steep gradient can only be present in the case of a past merger event, responsible of scattering the old MP component, followed by an *in situ* MR star formation from the infalling central gas.

It is, however, ambitious to derive robust conclusions about the progenitor of Sgr before it fell into the MW – whether it was a rotating discy galaxy or a pressure supported spheroidal galaxy – without ages or individual metallicities. We previously discussed how ages could help in getting a more complete picture of the evolution of Sgr. On the other hand, individual metallicities would give the possibility of quantifying the slope of the gradient and spotting possible brusque changes in its trend that we are not able to detect with our metallicity division. If we were able to quantify the radial metallicity gradient, we could compare it with similar pressure-supported dSphs but located in isolated environments. This comparison would enable us to evaluate the impact of both internal feedback and Sgr properties (such as mass and angular momentum) and exterior mechanisms on the Sgr metallicity gradient.

In our fits of the the spatial distributions of the MP and MR populations, the only significant difference we found was that of the scale radius, with the MR population being more centrally concentrated than the MP population. This reflects their spatial distribution and the detected trend in the [MP/MR] ratio: a younger, more centrally concentrated MR component is surrounded by an older, more disperse MP population present at increasing radii. To further disentangle the different processes which could have shaped the metallicity gradient in Sgr, the spatial properties should be accompanied by age information.

Besides the change in the scale radius between the MP and MR populations, if the other small differences we found in the structural parameters from the model fitting were real, what could they tell us? We found a small shift between the centres of the MR and MP populations in the RA direction. This could hint that the tidal interaction might have also played a more severe role in shaping and shifting the extended MP population compared to the MR population, which formed on a longer time-scale from the central gas reservoir. The change of the position angle for different metallicity populations could be related to the fact that they have interacted with the MW tidal field over different periods of time and thus their orbits and positions have evolved differently. It could also be due to rotation within the dwarf galaxy, which may be different for the young (MR) and the old (MP) populations, as suggested in for example Ibata et al. (1997). The values of the ellipticity for both populations (0.566 and 0.592 for MP and MR, respectively) are lower than the ellipticity of ~ 0.65 presented by Majewski et al. (2003). But it is still high, which is a sign of the process of tidal elongation of Sgr induced by interactions with the MW. The higher e value for the MR population might also be related to its lower velocity dispersion.

4.3.4 Comparison with other dSph

The Fornax dSph is an interesting example of a dwarf galaxy that shows some similarities with the Sgr dSph galaxy. The work of De Boer et al. (2012) reports the existence of a radial gradient of age and metallicity, with more MR and younger star-forming episodes condensed in the central region of the system, and oldest and more MP stars (with an age of ≥ 11 Gyr) appearing at all radii. The dominance of the intermediate-age stellar populations and the protracted SFH for both systems indicate that their dynamical masses were sufficient to retain enough gas (before the complete gas loss) to keep forming stars in their inner regions, after the gas fell back into the central potential well. It is also suggested that the cause of repeated peak in the star formation might be a merger with a gas-rich companion. In the case of Fornax, a precise chemical estimation

predicts the alpha-knee to occur at $[\text{Fe}/\text{H}] \sim -1.5$ (corresponding to an age of 7–10 Gyr). Battaglia et al. (2006) found the older, more MP population ($[\text{Fe}/\text{H}] < -1.3$, age > 10 Gyr) to be more spatially extended than the more MR and younger population (with $[\text{Fe}/\text{H}] > -1.3$ and ages between 2 and 8 Gyr), which was more centrally concentrated. Comparable results are presented in other works, such as Stetson, Hesser & Smecker-Hane (1998) and Wang et al. (2019). Also Coleman & de Jong (2008) and Del Pino et al. (2013) reported a protracted SFH and detected a gradient in the stellar populations of which the youngest and most MR formed more segregated in the centre of the galaxy.

Another compelling example is the Sculptor dSph galaxy, in which the MP ($[\text{Fe}/\text{H}] < -1.7$) and MR ($[\text{Fe}/\text{H}] > -1.7$) stellar components possess different kinematics and spatial distributions. I.e. the more extended metal-deficient population has higher velocity dispersion than the MR population (Tolstoy et al. 2004), which was likely created after the enriched original gas sank back to the centre.

4.4 New sample of very metal-poor stars in Sgr

Very and extremely MP stars in dwarf galaxies strongly reflect the early SFH of their host systems and, being tracers for the first nucleosynthesis events, can help to constrain the properties of the first stars, such as their initial mass function. The high-resolution study targeting the MP tail of Sgr performed by Hansen et al. (2018) discovered a similarity in the chemical composition between Sgr and the MW halo for these iron-depleted candidates, hinting that galaxies like Sgr contributed to the MW stellar halo. Hasselquist et al. (2017) reached a similar conclusion. By studying this type of objects, focusing on their chemical composition, it is possible to study the past and/or ongoing accretion events.

Despite the lack of abundances measurement, the distribution of our unprecedented selection of VMP stars opens a window into the star formation processes behind this ancient population. It suggests that no such stars were formed recently in the inner area, as we found them to be quite diffuse. Yet they do also show a higher density (similarly to the other populations) in the centre, as seen in Fig. 10. The distribution of this population can be linked to the gradual disruption of the progenitor, now leaving a core and the wide stellar streams. Indeed, it is also likely that tidal impulses, which Sgr experienced from the MW during passages at its pericentre, provoked a violent mixing of stars of different populations. This could have erased a possibly more pronounced radial metallicity profile in the Sgr progenitor, which was suspected to show an even greater fraction of more MR stars tightly bound in the interior regions (Chou et al. 2007). These stars would have been removed at later times compared to the older and more MP population, creating the known metallicity variations along the Sgr stellar streams (Chou et al. 2007; Hayes et al. 2020). Within this perspective, the remaining VMP objects in the core can be seen as left-overs of the more ancient population ($\gtrsim 10$ Gyr), once hosted in the galaxy progenitor, which has been gradually stripped away and deposited in the streams, known to be on average 1 dex more MP than the core (De Boer et al. 2015).

There is no overlap between our VMP selection and the APOGEE spectroscopic data (which contains mostly MR stars), while the cross-match with the PIGS spectroscopic catalogue reveals 115 stars in common. Additional spectroscopic follow-up spectroscopy of the VMP candidates in our sample is required to further study the nature of these stars and the early chemical evolution of Sgr, and this effort is ongoing.

5 CONCLUSIONS AND FUTURE WORK

In this work, we presented the largest photometric metallicity study of the core of the Sagittarius galaxy to date, using metallicity-sensitive narrow-band photometry from the PIGS. To summarize the results:

(i) By combining the PIGS photometry with the precise astrometry and broad-band photometry from *Gaia* EDR3, we were able to isolate bright giant Sgr stars ($G_0 \leq 17.3$) to build an unprecedented sample of 44 785 reliable Sgr members with metallicity information.

(ii) Using photometric instead of spectroscopic metallicities allows a much more homogeneous analysis of Sgr populations of varying metallicity. The PIGS data cover ~ 100 square degrees of Sgr out to 12 degrees along the semimajor axis from the centre (corresponding to ~ 5.5 kpc at the distance of Sgr), covering most of remnant of the dwarf galaxy core. We divided the Sgr stars into different metallicity populations, with our two main samples being the MP having $[\text{Fe}/\text{H}] < -1.3$ and the MR having $[\text{Fe}/\text{H}] > -1.0$.

(iii) Our data reveal a metallicity gradient, with the MR stars dominating in the inner regions and the MP stars towards the outer regions. This is consistent with previous evidence of a metallicity gradient in Sgr, but we extend it to much larger radii than previously observed.

(iv) We fitted models of the stellar density distributions for populations with various metallicities, separating MP and MR stars at $[\text{Fe}/\text{H}] = -2.0, -1.5, -1.3, \text{ and } -1.0$. The most striking difference we find is a change in the scale radius as function of metallicity, where the MR stars are more centrally concentrated, while the more MP component is more diffuse and distributed as a spheroid with a larger effective radius.

(v) The PIGS photometry is still sensitive to metallicity for VMP ($[\text{Fe}/\text{H}] < -2.0$) stars. We previously used it to select stars for low-/medium-resolution spectroscopic follow-up, resulting in the largest sample of 100 spectroscopically confirmed Sgr VMP stars. In this work, we further used the PIGS photometry to build an unprecedented sample of 1150 VMP candidates in Sgr with $G_0 < 17.3$. This remarkable sample of iron-depleted stars is left over from an ancient population that was once hosted in the Sgr progenitor, which has likely partially been removed and distributed to the Sgr streams and/or the Galactic halo.

(vi) We discussed how the history and evolution of Sgr could have impacted the various Sgr stellar populations. Our results are consistent with an outside-in quenching process with an older, diffuse MP stellar population and a younger, more centrally concentrated MR counterpart forming at later times. Sgr had an extended and rich SFH, forming different stellar populations with a different spatial and chemical evolution. To further connect our detected metallicity gradient with the properties of the underlying stellar populations, we need a better precision in metallicity and, currently missing, information about the ages of different MP populations.

Spectroscopic studies on elemental abundances of dwarf systems pave the way in revealing their assembly and evolution histories in more depth, and increase the knowledge about metallicity distributions and age gradients in dwarf galaxies. For example, a strong connection exists between the initial mass function and the early chemical evolution. Chemical information allows to shed light on important aspects in the life of a dwarf galaxy, such as the frequency of star formation episodes, the stellar yields, and the mixing processes that took place in the interstellar medium. Another factor in the evolution of a dwarf galaxy is its interactions with other galaxies, and Sgr is a unique example of a complex disrupting dwarf system (core and streams).

By exploring with high-resolution spectroscopy the chemical composition of the Sgr stellar populations, especially focusing on its MP tail, it will be possible to constrain its SFH and characterize the early evolution of this dSph galaxy. We are planning spectroscopic follow-up of our unprecedented Sgr sample with metallicity information, the result of the powerful combination of the metallicity-sensitive photometry from the *Pristine* survey (Starkenburger et al. 2017), and the excellent *Gaia* EDR3 data.

ACKNOWLEDGEMENTS

We would like to thank the reviewer for carefully reading the manuscript and giving many valuable suggestions.

We thank the PIGS Anglo-Australian Telescope (AAT) observers Sven Buder, Geraint Lewis, Sarah Martell, Jeffrey Simpson, Zhen Wan, and Daniel Zucker.

We thank the Australian Astronomical Observatory, which has made these observations possible. We acknowledge the traditional owners of the land on which the AAT stands, the Gamilaraay people, and pay our respects to elders past and present. Based on data obtained at Siding Spring Observatory (via programs S/2017B/01, A/2018A/01, OPTICON 2018B/029, and OPTICON 2019A/045, PI: A. Arentsen and A/2020A/11, PI: D. B. Zucker).

Based on observations obtained with MegaPrime/MegaCam, a joint project of CFHT and CEA/DAPNIA, at the Canada-France-Hawaii Telescope (CFHT), which is operated by the National Research Council (NRC) of Canada, the Institut National des Sciences de l'Univers of the Centre National de la Recherche Scientifique (CNRS) of France, and the University of Hawaii.

AA, NFM, and ZY gratefully acknowledge funding from the European Research Council (ERC) under the European Unions Horizon 2020 research and innovation programme (grant agreement No. 834148).

ES acknowledges funding through VIDI grant 'Pushing Galactic Archaeology to its limits' (with project number VI.Vidi.193.093) which is funded by the Dutch Research Council (NWO)

PJ acknowledges financial support of FONDECYT Regular Grant Number 1200703.

P.J. and S.V. thank the Millenium Nucleus ERI NCN2021.017.

GK, NFM, RI, VH, and ZY gratefully acknowledge support from the French National Research Agency (ANR) funded project 'Pristine' (ANR-18-CE31-0017).

JIGH acknowledges financial support from the Spanish Ministry of Science and Innovation (MICINN) project PID2020-117493GB-I00.

DA acknowledges support from ERC Starting Grant NEFERTITI H2020/808240.

This project has received funding from the European Union's Horizon 2020 research and innovation programme under grant agreement no. 730890. This material reflects only the authors views and the Commission is not liable for any use that may be made of the information contained therein.

The authors thank the International Space Science Institute, Bern, Switzerland for providing financial support and meeting facilities to the international team 'Pristine'.

This work has made use of data from the European Space Agency (ESA) mission *Gaia* (<https://www.cosmos.esa.int/gaia>), processed by the *Gaia* Data Processing and Analysis Consortium (DPAC, <https://www.cosmos.esa.int/web/gaia/dpac/consortium>). Funding for the DPAC has been provided by national institutions, in particular the institutions participating in the *Gaia* Multilateral Agreement.

Funding for the Sloan Digital Sky Survey (SDSS) IV has been provided by the Alfred P. Sloan Foundation, the U.S. Department of Energy Office of Science, and the Participating Institutions. SDSS acknowledges support and resources from the Center for High-Performance Computing at the University of Utah. The SDSS website is www.sdss.org.

SDSS is managed by the Astrophysical Research Consortium for the Participating Institutions of the SDSS Collaboration including the Brazilian Participation Group, the Carnegie Institution for Science, Carnegie Mellon University, Center for Astrophysics | Harvard & Smithsonian (CfA), the Chilean Participation Group, the French Participation Group, Instituto de Astrofísica de Canarias, The Johns Hopkins University, Kavli Institute for the Physics and Mathematics of the Universe (IPMU) / University of Tokyo, the Korean Participation Group, Lawrence Berkeley National Laboratory, Leibniz Institut für Astrophysik Potsdam (AIP), Max-Planck-Institut für Astronomie (MPIA Heidelberg), Max-Planck-Institut für Astrophysik (MPA Garching), Max-Planck-Institut für Extraterrestrische Physik (MPE), National Astronomical Observatories of China, New Mexico State University, New York University, University of Notre Dame, Observatório Nacional / MCTI, The Ohio State University, Pennsylvania State University, Shanghai Astronomical Observatory, United Kingdom Participation Group, Universidad Nacional Autónoma de México, University of Arizona, University of Colorado Boulder, University of Oxford, University of Portsmouth, University of Utah, University of Virginia, University of Washington, University of Wisconsin, Vanderbilt University, and Yale University.

Based on observations made with the Canada-France-Hawaii Telescope (CFHT) and the Anglo-Australian Telescope (AAT).

DATA AVAILABILITY

The data underlying this article will be shared on reasonable request to the corresponding author.

REFERENCES

- Abdurro Uf et al., 2022, *ApJS*, 259, 35
Aguado D. S. et al., 2019, *MNRAS*, 490, 2241
Ahumada R. et al., 2020, *ApJS*, 249, 3
Alard C., 2001, *A&A*, 377, 389
Alfaro-Cuello M. et al., 2020, *ApJ*, 892, 20
Allende Prieto C., Beers T. C., Wilhelm R., Newberg H. J., Rockosi C. M., Yanny B., Lee Y. S., 2006, *ApJ*, 636, 804
Arentsen A. et al., 2020, *MNRAS*, 496, 4964
Arentsen A. et al., 2021, *MNRAS*, 505, 1239
Battaglia G. et al., 2006, *A&A*, 459, 423
Bellazzini M., Ferraro F. R., Buonanno R., 1999a, *MNRAS*, 304, 633
Bellazzini M., Ferraro F. R., Buonanno R., 1999b, *MNRAS*, 307, 619
Bellazzini M., Correnti M., Ferraro F. R., Monaco L., Montegriffo P., 2006, *A&A*, 446, L1
Bellazzini M. et al., 2008, *AJ*, 136, 1147
Bellazzini M., Ibata R., Malhan K., Martin N., Famaey B., Thomas G., 2020, *A&A*, 636, A107
Belokurov V. et al., 2014, *MNRAS*, 437, 116
Benítez-Llambay A., Navarro J. F., Abadi M. G., Gottlöber S., Yepes G., Hoffman Y., Steinmetz M., 2016, *MNRAS*, 456, 1185
Bland-Hawthorn J., Gerhard O., 2016, *ARA&A*, 54, 529
Bonifacio P., Hill V., Molaro P., Pasquini L., Di Marcantonio P., Santin P., 2000, *A&A*, 359, 663
Bullock J. S., Johnston K. V., 2005, *ApJ*, 635, 931
Burton W. B., Lockman F. J., 1999, *A&A*, 349, 7
Carrera R., Gallart C., Aparicio A., Hardy E., 2011, *AJ*, 142, 61
Carretta E. et al., 2010a, *A&A*, 520, A95
Carretta E. et al., 2010b, *ApJ*, 714, L7
Casagrande L. et al., 2021, *MNRAS*, 507, 2684
Chiti A., Frebel A., 2019, *ApJ*, 875, 112
Chiti A., Hansen K. Y., Frebel A., 2020, *ApJ*, 901, 164
Chou M.-Y. et al., 2007, *ApJ*, 670, 346
Coleman M. G., de Jong J. T. A., 2008, *ApJ*, 685, 933
De Boer T. J. L. et al., 2012, *A&A*, 544, A73
De Boer T. J. L., Belokurov V., Beers T. C., Lee Y. S., 2014, *MNRAS*, 443, 658
De Boer T. J. L., Belokurov V., Koposov S., 2015, *MNRAS*, 451, 3489
Del Pino A., Hidalgo S. L., Aparicio A., Gallart C., Carrera R., Monelli M., Buonanno R., Marconi G., 2013, *MNRAS*, 433, 1505
del Pino A., Aparicio A., Hidalgo S. L., 2015, *MNRAS*, 454, 3996
del Pino A., Łokas E. L., Hidalgo S. L., Fouquet S., 2017, *MNRAS*, 469, 4999
Del Pino A., Fardal M. A., van der Marel R. P., Łokas E. L., Mateu C., Sohn S. T., 2021, *ApJ*, 908, 244
Fabricius C. et al., 2021, *A&A*, 649, A5
Ferguson P. S., Strigari L. E., 2020, *MNRAS*, 495, 4124
Fernández-Alvar E. et al., 2021, *MNRAS*, 508, 1509
Frebel A., Bromm V., 2012, *ApJ*, 759, 115
Gaia Collaboration, 2021, *A&A*, 649, A1
Garro E. R., Minniti D., Gómez M., Alonso-García J., 2021, *A&A*, 654, A23
Goldsbury R., Richer H. B., Anderson J., Dotter A., Sarajedini A., Woodley K., 2010, *AJ*, 140, 1830
Hansen C. J., El-Souri M., Monaco L., Villanova S., Bonifacio P., Caffau E., Sbordone L., 2018, *ApJ*, 855, 83
Harris W. E., 1996, *AJ*, 112, 1487
Harris W. E. et al., 2010, preprint ([arXiv:1012.3224](https://arxiv.org/abs/1012.3224))
Hasselquist S. et al., 2017, *ApJ*, 845, 162
Hayes C. R. et al., 2020, *ApJ*, 889, 63
Helmi A., 2020, *ARA&A*, 58, 205
Hyde E. A. et al., 2015, *ApJ*, 805, 189
Ibata R., 1997, HST Proposal ID 7463. Cycle 7, 7463
Ibata R. A., Gilmore G., Irwin M. J., 1994, *Nature*, 370, 194
Ibata R. A., Wyse R. F. G., Gilmore G., Irwin M. J., Suntzeff N. B., 1997, *AJ*, 113, 634
Ibata R., Lewis G. F., Irwin M., Totten E., Quinn T., 2001, *ApJ*, 551, 294
Keller S. C., Yong D., Da Costa G. S., 2010, *ApJ*, 720, 940
Kirby E. N., Cohen J. G., Guhathakurta P., Cheng L., Bullock J. S., Gallazzi A., 2013, *ApJ*, 779, 102
Koribalski B., Johnston S., Otrupcek R., 1994, *MNRAS*, 270, L43
Law D. R., Majewski S. R., 2010, *ApJ*, 714, 229
Layden A. C., Sarajedini A., 2000, *AJ*, 119, 1760
Lewis I. J. et al., 2002, *MNRAS*, 333, 279
Li H., Tan K., Zhao G., 2018, *ApJS*, 238, 16
Lindgren L. et al., 2021, *A&A*, 649, A2
Łokas E. L., Kazantzidis S., Majewski S. R., Law D. R., Mayer L., Frinchaboy P. M., 2010, *ApJ*, 725, 1516
Majewski S. R., Skrutskie M. F., Weinberg M. D., Ostheimer J. C., 2003, *ApJ*, 599, 1082
Malhan K. et al., 2022, *ApJ*, 926, 107
Martin N. F., de Jong J. T. A., Rix H.-W., 2008, *ApJ*, 684, 1075
Mateo M., Olszewski E. W., Morrison H. L., 1998, *ApJ*, 508, L55
Mayer L., Governato F., Colpi M., Moore B., Quinn T., Wadsley J., Stadel J., Lake G., 2001, *ApJ*, 559, 754
Mayer L., Mastropietro C., Wadsley J., Stadel J., Moore B., 2006, *MNRAS*, 369, 1021
McDonald I. et al., 2013, *MNRAS*, 436, 413
McWilliam A., Wallerstein G., Mottini M., 2013, *ApJ*, 778, 149
Mercado F. J. et al., 2021, *MNRAS*, 501, 5121
Monaco L., Bellazzini M., Ferraro F. R., Pancino E., 2003, *ApJ*, 597, L25
Monaco L., Pancino E., Ferraro F. R., Bellazzini M., 2004, *MNRAS*, 349, 1278
Monaco L., Bellazzini M., Bonifacio P., Ferraro F. R., Marconi G., Pancino E., Sbordone L., Zaggia S., 2005, *A&A*, 441, 141

Mottini M., Wallerstein G., McWilliam A., 2008, *AJ*, 136, 614
 Mucciarelli A., Bellazzini M., Ibata R., Romano D., Chapman S. C., Monaco L., 2017, *A&A*, 605, A46
 Niederste-Ostholt M., Belokurov V., Evans N. W., Peñarrubia J., 2010, *ApJ*, 712, 516
 Oria P.-A., Ibata R., Ramos P., Famaey B., Errani R., 2022, *ApJ*, 932, L14
 Peñarrubia J., Belokurov V., Evans N. W., Martínez-Delgado D., Gilmore G., Irwin M., Niederste-Ostholt M., Zucker D. B., 2010, *MNRAS*, 408, L26
 Revaz Y., Jablonka P., 2018, *A&A*, 616, A96
 Riello M. et al., 2021, *A&A*, 649, A3
 Ruiz-Lara T., Gallart C., Bernard E. J., Cassisi S., 2020, *Nature Astron.*, 4, 965
 Rybizki J. et al., 2022, *MNRAS*, 510, 2597
 Sales L. V., Helmi A., Battaglia G., 2010, *Adv. Astron.*, 2010, 194345
 Saunders W. et al., 2004, in Moorwood A. F. M., Iye M., eds, Proc. SPIE Conf. Ser., Vol. 5492, Ground-based Instrumentation for Astronomy. SPIE, Bellingham, p. 389
 Sbordone L., Bonifacio P., Marconi G., Buonanno R., Zaggia S., 2005, *A&A*, 437, 905
 Schlegel D. J., Finkbeiner D. P., Davis M., 1998, *ApJ*, 500, 525
 Sharp R. et al., 2006, in McLean I. S., Iye M., eds, Proc. SPIE Conf. Ser. Vol. 6269, Ground-based and Airborne Instrumentation for Astronomy. SPIE, Bellingham, p. 62690G
 Siegel M. H. et al., 2007, *ApJ*, 667, L57
 Smecker-Hane T. A., McWilliam A., 2002, preprint ([arXiv:astro-ph/0205411](https://arxiv.org/abs/astro-ph/0205411))
 Sollima A., Carretta E., D’Orazi V., Gratton R. G., Bragaglia A., Lucatello S., 2014, *MNRAS*, 443, 1425
 Starkenburg T. K., Helmi A., 2015, *A&A*, 575, A59
 Starkenburg E. et al., 2017, *MNRAS*, 471, 2587
 Stetson P. B., Hesser J. E., Smecker-Hane T. A., 1998, *PASP*, 110, 533
 Taibi S., Battaglia G., Leaman R., Brooks A., Riggs C., Munshi F., Revaz Y., Jablonka P., 2022, preprint ([arXiv:2206.08988](https://arxiv.org/abs/2206.08988))
 Tepper-García T., Bland-Hawthorn J., 2018, *MNRAS*, 478, 5263
 Tolstoy E. et al., 2004, *ApJ*, 617, L119
 Vasiliev E., Belokurov V., 2020, *MNRAS*, 497, 4162
 Wang M. Y. et al., 2019, *ApJ*, 881, 118

Yanny B. et al., 2009, *AJ*, 137, 4377
 Youakim K. et al., 2017, *MNRAS*, 472, 2963

APPENDIX A: THE EFFECT OF ALPHA ABUNDANCES ON THE CCD

The *Pristine* colour–colour diagram has been shown to be metallicity-sensitive (Starkenburg et al. 2017), but while writing the current work, we discovered that there is also an effect due to the alpha abundances, especially for cooler stars. For this investigation, we used APOGEE abundances for giant stars in the main *Pristine* survey and in Sgr, with ASPCAPFLAG = 0 and uncertainties on $[\alpha/M] < 0.1$ dex. In the top panel of Fig. A1, we present the different $[M/H]$ versus $[\alpha/M]$ sequences between Sgr (red) and the training sample (black). The latter is split into two sequences at higher metallicity, representing thin and thick disc stars.

We make three different metallicity bin selections, indicated by the grey vertical lines, and plot their colour–colour diagrams in the bottom panels of Fig. A1, colour-coded by their alpha abundances. For $(BP - RP)_0 > 1.5$, there are clearly three different $[\alpha/M]$ sequences in each of these colour–colour diagrams. For $(BP - RP)_0 < 1.5$, the situation is less clear. In the two more MP bins, the thin- and thick-disc stars overlap, but in the most MR bin there still appears to be some separation between them. Unfortunately, there are practically no Sgr stars in APOGEE with $(BP - RP)_0 < 1.5$, so it is unclear whether they would overlap with the thin- and thick-disc stars in any of the metallicity bins.

Although calcium is an alpha element, the Ca II H&K lines closely trace the metallicity of most stars, down to the extremely MP regime (Starkenburg et al. 2017). The stars with $(BP - RP)_0 > 1.5$ have temperatures in the range of 3800–4200 K. We conclude that for giant stars of these temperatures the metallicity-sensitivity of the Ca II H&K lines apparently breaks down – they start to trace the alpha abundance instead.

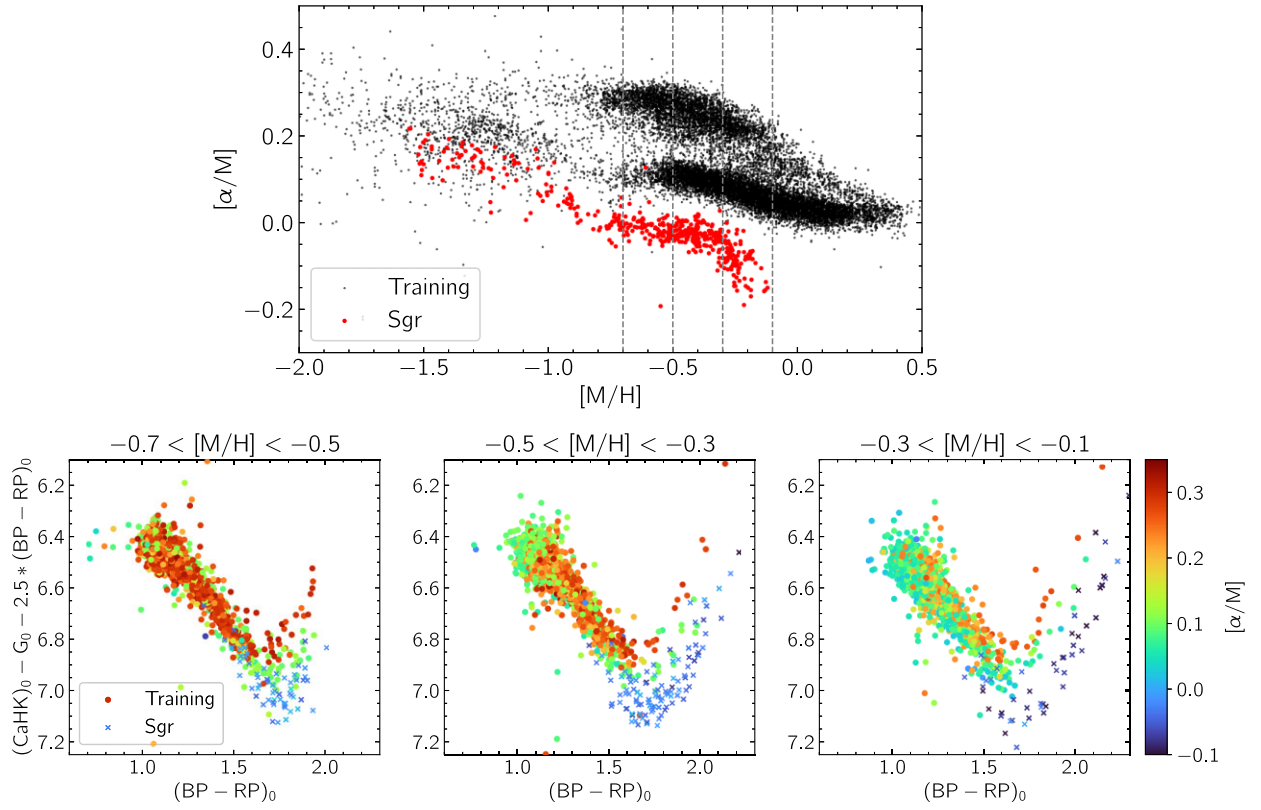


Figure A1. Top: distribution of $[M/H] - [\alpha/M]$ among APOGEE stars in the *Pristine* training sample and Sgr. Bottom: *pristine* colour–colour diagram for three different metallicity ranges (see titles and grey lines in the top panel), colour-coded by $[\alpha/M]$. For $(\text{BP} - \text{RP})_0 > 1.5$, three different $[\alpha/M]$ sequences can clearly be seen.

This paper has been typeset from a $\text{\TeX}/\text{\LaTeX}$ file prepared by the author.